Sensitivity of the two-dimensional shearless mixing layer to the initial turbulent kinetic energy and integral length scale

M. Fathali* and M. Khoshnami Deshiri

Department of Aerospace Engineering, K.N. Toosi University of Technology, Tehran, Iran

(Received 11 October 2015; revised manuscript received 27 December 2015; published 20 April 2016)

The shearless mixing layer is generated from the interaction of two homogeneous isotropic turbulence (HIT) fields with different integral scales ℓ_1 and ℓ_2 and different turbulent kinetic energies E_1 and E_2. In this study, the sensitivity of temporal evolutions of two-dimensional, incompressible shearless mixing layers to the parametric variations of ℓ_1/ℓ_2 and E_1/E_2 is investigated. The sensitivity methodology is based on the nonintrusive approach; using direct numerical simulation and generalized polynomial chaos expansion. The analysis is carried out at $\mathrm{Re}_{\ell_1} = 90$ for the high-energy HIT region and different integral length scale ratios $1/4 \leqslant \ell_1/\ell_2 \leqslant 4$ and turbulent kinetic energy ratios $1 \leqslant E_1/E_2 \leqslant 30$. It is found that the most influential parameter on the variability of the mixing layer evolution is the turbulent kinetic energy while variations of the integral length scale show a negligible influence on the flow field variability. A significant level of anisotropy and intermittency is observed in both large and small scales. In particular, it is found that large scales have higher levels of intermittency and sensitivity to the variations of ℓ_1/ℓ_2 and E_1/E_2 compared to the small scales. Reconstructed response surfaces of the flow field intermittency and the turbulent penetration depth show monotonic dependence on ℓ_1/ℓ_2 and E_1/E_2. The mixing layer growth rate and the mixing efficiency both show sensitive dependence on the initial condition parameters. However, the probability density function of these quantities shows relatively small solution variations in response to the variations of the initial condition parameters.

DOI: 10.1103/PhysRevE.93.043122

I. INTRODUCTION

Turbulent mixing occurs in a wide variety of geophysical flows as well as in many industrial and energy-related applications. Turbulent mixing might be essentially considered a process involving stretching and folding of material lines or surfaces which is accompanied by the spatiotemporal chaotic motion of the turbulent flow. The chaotic aspect of these stretching-folding processes results in extremely intricate trajectories for flow particles, which drastically modify flow field transport properties compared to those in a laminar state.

Due to the chaotic nature of the turbulent mixing, this process can show extreme sensitivity to the variations of the specifying flow field parameters at the initial or upstream flow field. This sensitive dependence of the turbulent mixing process, both in the transitional period and the asymptotic states, to the upstream or initial condition has been the subject of many studies [1,2].

Besides initial or upstream flow field parameters, dynamics of the chaotic motion and consequently hydrodynamical mixing can be drastically influenced by the reduction of the space dimensionality. In turbulence, it is well known that the reduction of the physical space dimension from the relevant value 3 to 2 results in an energy-enstrophy double cascade, i.e., an inverse cascade of the kinetic energy to large scales and a direct cascade of enstrophy to small scales. Therefore, two-dimensional turbulence can show qualitatively and quantitatively different dynamics compared to its three-dimensional turbulence counterpart. Although two-dimensional turbulence is an idealized configuration, the inverse cascade can be observed in many three-dimensional turbulent flows such as the rotating fluid turbulence, magnetohydrodynamic turbulence, and geophysical flows in atmosphere, oceans, and magnetosphere. This issue is one of the main motivations behind the enormous amount of research which has been done on the two-dimensional turbulence (see among others Ref. [3–5], and an extensive review of experiment research can be found in Ref. [6]).

To investigate the abstract nature of the hydrodynamical mixing process, two canonical flow field configurations are mainly considered which are depicted in Fig. 1, i.e., shear mixing layer and shearless (or shear-free) mixing layer. In the shear mixing layer, two initially separated and parallel streams with different mean velocities are merged and form a mixing layer in which intense mixing process occurs in the velocity-gradient region between the two free streams [7]. The shearless mixing layer is formed in a decaying grid turbulence in which the mean velocity is constant throughout but two different homogenous isotropic turbulent (HIT) regions are formed on either side of the stream. As the flow evolves, energetic large eddies from these two HIT fields penetrate and diffuse into one another and form an anisotropic mixing region [8].

Since flows encountered in nature or industrial applications are more often accompanied by shear, the shear mixing layer has been extensively investigated both in three dimensions (see Refs. [1,9–13]) and in two dimensions (see Refs. [14–18]), just to name a few. Concisely, in this experimental and numerical research, the impact of the turbulent intensity, energy spectrum, Reynolds-stress tensor, integral length scales of the upstream and initial velocity fluctuations, as well as the dynamics of the coherent vortical structures on the shear mixing layer evolution have been examined.

However, concerning the turbulent mixing process, the shearless mixing layer has two distinguishing features compared to the shear mixing layer. First, in the latter flow field configuration, the turbulent mixing process can be

*mfathali@kntu.ac.ir

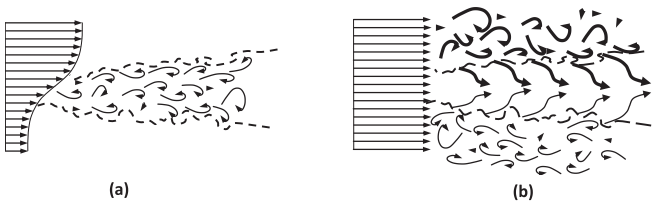

FIG. 1. Schematic of the spatially evolving mixing layer. (a) Shear mixing layer; (b) shearless mixing layer.

overwhelmed by the mean shear effects such as the turbulent production or entrainment flow caused by the Kelvin-Helmholtz instability. In the shearless mixing layer, due to the absence of the mean shear, dynamics and kinematics of turbulent mixing are isolated from the above-mentioned mechanisms. Therefore, in the shearless mixing layer, it is possible to investigate the fundamental aspects of the mixing process, which is exclusively originated from turbulence-turbulence interactions.

The second issue is related to the impact of the variation of the space dimensionality on the turbulent mixing layer evolution. It is well known that flow field evolutions of both shear and shearless mixing layers are profoundly influenced by the dynamics of the coherent energetic eddies [19,20]. In the shear mixing layer, these energetic eddies mainly originate from the Kelvin-Helmholtz instability, which is originally a two-dimensional phenomenon. Therefore, one might expect qualitatively similar features between the two- and three-dimensional shear mixing layers evolutions.

In the shearless mixing layer, on the other hand, these influential energetic eddies originate from the dynamics of the interacting HIT regions, which, due to the existence of the dual cascade, are significantly affected by the space dimensionality. Therefore, it is expected that, in contrast to the shear mixing layer, two- and three-dimensional shearless mixing layers show nontrivially different dynamics.

Notably, in spite of the fundamental differences between dynamics of the two- and three-dimensional shearless mixing layers, almost all research has been carried out three dimensionally. The first experimental investigation of a shearless mixing layer was carried out by Gilbert [21]. In this experiment, the impact of the turbulent kinetic energy ratio of two interacting HIT regions on the growth rate of the mixing layer is investigated. This study discerns no significant deviation from Gaussian statistics for the velocity inside the mixing region.

In a later experimental study, Veeravalli and Warhaft investigated the combined effects of the integral length scale and turbulent kinetic energy ratios of two HIT regions on the shearless mixing layer evolution [8]. In contrast to the previous experiment, a pronounced deviation from Gaussian distribution was observed by examining the velocity skewness and flatness coefficients. They also found that the penetration of energetic eddies from the high-energy HIT region into the low-energy one is the primary mechanism of mixing.

In the first numerical study of the shearless mixing layer, Briggs *et al.* investigated the effect of the low-wave-number part of the initial energy spectrum (coherent vortical structures) on the subsequent mixing layer growth, using the direct numerical dimulation (DNS) approach [19]. Consistent with the experimental results of Veeravalli and Warhaft [8], this numerical study revealed that the primary source of the mixing layer growth, departure from Gaussianity, and energy transport into the mixing layer is penetrations of eddies with the size of $(k^{3/2}/\varepsilon)$, known as energetic eddies.

In a later numerical study, Knaepen *et al.* more accurately investigated this departure from Gaussianity inside the mixing layer, using both large-eddy simulation (LES) and DNS approaches [22]. They also found that this non-Gaussian velocity statistics is entirely produced by the transport mechanisms, which can be accurately predicted by both LES and DNS approaches.

In another numerical study, Tordella and Iovieno investigated the impact of the kinetic energy and integral length-scale ratios of the two interacting HIT fields on the Gaussian asymptotic state and extent of the mixing region [23]. In comparison to the experimental research of Veeravalli and Warhaft [8], in this numerical study a wider range of the turbulent kinetic energy and length-scale ratios was considered. They observed that the intermittency level and the growth of the mixing region are amplified by imposing concordant kinetic energy and integral length-scale gradients across the mixing layer.

Kang and Meneveau conducted both numerical and experimental studies on the shearless mixing layer with Reynolds numbers considerably higher than those of prior studies [24]. They found that the dominant effect of the large-scale motions on the deviations from Gaussianity persists in high-Reynolds-number regimes. In the same line as in the numerical studies, Tordella and Iovieno found that even small-scale structures in the mixing region show a nontrivial level of anisotropy and departure from Gaussianity [25]. In a more recent DNS study by the same authors, it was observed that only the existence of the integral length-scale difference between two interacting HIT fields can develop intermittency and departure from Gaussianity in the subsequent mixing layer evolution [26].

Recently, as the only documented study on the two-dimensional shearless mixing layer, Iovieno *et al.* investigated the mixing of a passive scalar in two- and three-dimensional shearless mixing layers [27]. In this research, they reported the mixing layer growth as well as the evolutions of the mean profiles of the passive scalar and its variances. Moreover, they found significant differences in the passive scalar diffusion and the propagation of the intermittent layers in two and three dimensions.

Considering very limited reported results about the two-dimensional shearless mixing layer and the fact that the shearless mixing layer involves essentially different mechanisms in its two- and three-dimensional evolutions, this research focuses on the further investigation of the two-dimensional shearless mixing layer. The objective of the present study is to address the sensitivity of a two-dimensional shearless mixing layer evolution to the parametric variations of the integral length scale and turbulent kinetic energy ratios of two interacting HIT fields. More specifically, this research aims at identifying the impact of these controlling parameters on the (1) intermittency and departure from Gaussian statistics inside the mixing region, (2) energy transfer mechanisms into the mixing region, and (3) the mixing process in a decaying

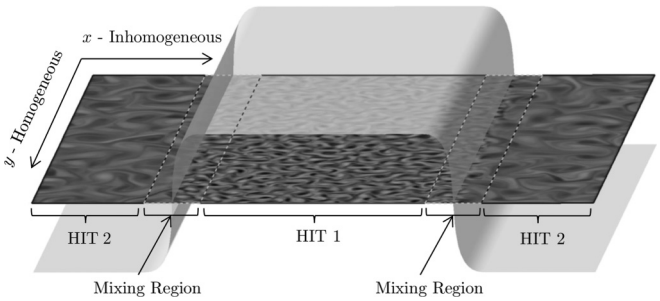

FIG. 2. Graphical representation of the initial flow field configuration consisting of two shearless mixing layers. The transparent surface depicts matching profile.

temporal two-dimensional shearless mixing layer, using the DNS approach.

It should be noted that the considered controlling parameters, i.e., the integral length scale and the turbulent kinetic energy, are closely related to the low wave-number part of the energy spectrum which influences the motion of the coherent energetic eddies in the shearless mixing layer [23].

The remainder of the paper is organized as follows. First, in Sec. II, the methodology of the sensitivity analysis, the governing equations, and flow field configuration and its initialization are briefly explained. Next, in Sec. III, results of the sensitivity analysis are presented. Finally, some conclusions are summarized in Sec. IV.

II. SENSITIVITY ANALYSIS: FORMULATION OF THE STOCHASTIC SYSTEM

Among a variety of methods for sensitivity analysis, in this study a nonstatistical approach based on the nonintrusive generalized polynomial chaos (gPC) expansion is used [28–32].

Here, controlling flow field parameters are considered as independent random variables $\mathscr{L}$ and $\mathscr{E}$,

$$\mathscr{L} \equiv \frac{\ell_1}{\ell_2}, \quad \text{and} \quad \mathscr{E} \equiv \frac{E_1}{E_2}, \tag{1}$$

where ℓ and E are respectively initial integral length scale and initial turbulent kinetic energy, and indices 1 and 2 refer to the interacting HIT regions 1 and 2 (see Fig. 2). Therefore, the evolution of the shearless mixing layer may be considered as a function of independent random variables $\mathscr{L}$ and $\mathscr{E}$ in addition to the existing physical spatiotemporal variables $\mathbf{x}$ and t, i.e.,

$$\partial_t u(\mathbf{x},t;\mathscr{L},\mathscr{E}) = \mathcal{NS}(u), \tag{2}$$

where u presents any flow field variable, $\mathcal{NS}$ stands for the NS equation operator which describes the dynamics of an incompressible viscous fluid flow on the spatial domain $D \subset \mathbb{R}^2$ and time interval $(0,T]$. Extra dimensions $\mathscr{L}$ and $\mathscr{E}$ are defined within the square domain sample space $1 \leqslant \mathscr{E} \leqslant 30$ and $1/4 \leqslant \mathscr{L} \leqslant 4$ with certain probability distribution. The methodology of the sensitivity analysis may be concisely expressed as follows.

By parametric variations of $\mathscr{L}$ and $\mathscr{E}$, a set of $N_q = n_{\mathscr{L}} \times n_{\mathscr{E}}$ individual quadrature nodes $(\mathscr{L}_i,\mathscr{E}_i)$ in the $\mathscr{L}$-$\mathscr{E}$ plane is generated. Since in each of these quadrature nodes the value of $\mathscr{L}$ and $\mathscr{E}$ is specified, the dynamical system (2) can be integrated in time, using any deterministic NS solver, to produce the corresponding sample solution $u(\mathbf{x},t;\mathscr{L}_i,\mathscr{E}_i)$.

Having obtained sample solutions $u(\mathbf{x},t;\mathscr{L}_i,\mathscr{E}_i)$ at all quadrature nodes, an interpolate response surface in the $\mathscr{L}$-$\mathscr{E}$ plane can be constructed based on the gPC to establish an explicit relation between evolution of any flow field variable $u(\mathbf{x},t;\mathscr{L},\mathscr{E})$ and controlling parameters $\mathscr{L}$ and $\mathscr{E}$.

In this research, $n_{\mathscr{L}} = n_{\mathscr{E}} = 11$ different values of $\mathscr{L}$ and $\mathscr{E}$ are considered, which results in $N_q = 121$ quadrature nodes. The flow field initialization of the NS equation at each N_q quadrature node and the numerical solution method are presented in Sec. II A. In Sec. II B, the reconstruction of the response surface using orthogonal gPC basis is given.

A. Flow field configuration, initialization, and method of solution

To perform DNS at each $N_q = 121$ quadrature node, a properly calibrated initial condition is required. To enforce the periodicity, which is required from the numerical point of view, the flow field configuration is considered as two shearless mixing layers which are placed side by side along the inhomogeneous direction x and are performing reverse transitions compared to each other, as depicted in Fig. 2. The shearless mixing layer consists of two distinct HIT fields 1 and 2, with different turbulent kinetic energies and integral length scales, which are matched through a rapid transition layer as follows:

$$\omega(x,y) = (1 - f(x))^{\frac{1}{2}}\omega_2(x,y) + f(x)^{\frac{1}{2}}\omega_1(x,y), \tag{3}$$

where $\omega_1(x,y)$ and $\omega_2(x,y)$ are respectively two HIT vorticity fields 1 and 2. The matching function $f(x)$ is

$$f(x) = \frac{1}{2}\left[1 + p(0)p\left(\frac{L}{4}\right)p\left(\frac{3L}{4}\right)\right], \tag{4}$$
$$p(\xi) = \tanh\left(c\frac{x-\xi}{L}\right),$$

where L is the size of the computational domain. The constant c determines the transitional layer thickness and is set as $c = 1000$ to ensure that matching is made over a layer with a width of the same order as the smallest flow field integral length scale, i.e., $L/800$. It should be noted that since vorticity fields are merged in Eq. (3), the matching process does not destroy the divergence freeness of the resulted initial velocity field.

Each HIT vorticity field is generated in Fourier space with the following amplitudes:

$$\widehat{\omega}(k_x,k_y,0) = \left[\frac{k^2 E_s(k,0)}{\pi}\right]^{1/2}\exp(i\theta), \tag{5}$$

where $i = \sqrt{-1}$, the random phase is denoted by $\theta \in [0,2\pi]$ with uniform probability distribution, and $E_s(k,0)$ is an initial energy spectrum

$$E_s(k,0) = \frac{1}{k_p}\left(\frac{k}{k_p}\right)^7 \exp\left[-3.5\left(\frac{k}{k_p}\right)^2\right], \tag{6}$$

where $k^2 = k_x^2 + k_y^2$ is the spectral radius [33]. Moreover, k_p is the peak wave number which, in two-dimensional turbulence,

is related to the length scale [33–35],

$$\ell = \left(\frac{\int_0^\infty E_s(k)dk}{\int_0^\infty k^2 E_s(k)dk} \right)^{1/2} = \sqrt{\frac{7}{8}} k_p^{-1}. \quad (7)$$

There is a discrepancy for the interpretation of this length scale in Refs. [33–35]. Chasnov [33] considered this length scale, which is closely related to the Taylor length scale, as the microscale length scale. On the contrary, in Refs. [34,35] this length scale is attributed to the integral length scale, which may be defined as $L_{\text{int}} = \int_0^\infty k^{-1} E_s(k)dk / \int_0^\infty E_s(k)dk$ [36, p. 55]. Here, following Refs. [34,35], the length scale (7) is considered as the integral length scale. However, it can be easily shown that for the specific energy spectrum (6), the length scale (7) and the integral length scale L_{int} are in the same order, i.e., $L_{\text{int}} = 1.13\ell$.

The reconstruction of each HIT vorticity field is followed by a freely decay development run until a mature spectrum with physical phase relation among different Fourier modes is established. Since during this development run the integral length scale increases, to restore the desired length scale ℓ the peak wave number k_p in the initial energy spectrum (6) is set as 0.9ℓ. Depending on the desired integral length scale, this adjustment evolution approximately endures between 5τ to 10τ, where $\tau = t\ell/\sqrt{E}$ is the number of eddy turnovers at time t. Afterwards, Fourier amplitudes of the time-evolved HIT field are rescaled in order to match the prescribed initial turbulent kinetic energy E.

To generate initial shearless mixing layers corresponding to $N_q = 121$ quadrature nodes, the turbulent kinetic energy and the length scale of the HIT region 1 are kept constant as $\ell_1 = L/200$ and $E_1 = 2.5$ in arbitrary units while turbulent kinetic energy and the length scale of the HIT region 2 are varied as $\ell_1/4 \leqslant \ell_2 \leqslant 4\ell_1$ and $E_1/30 \leqslant E_2 \leqslant E_1$.

The upper bounds of these intervals are set based on the resolution as well as the computational domain size considerations. However, performing a few numerical experiments with higher values of $\mathscr{L}$ and $\mathscr{E}$ revealed that further increasing the ranges of these intervals does not lead to a considerably higher level of the flow field variability.

Moreover, in order to examine the diffusion of the passive scalar interface across the turbulent mixing region, the passive scalar $Z \in [0;1]$ is also introduced into the flow field. The passive scalar concentration is initially uniform in the two isotropic regions, $Z = 1$ in the HIT region 1 and $Z = 0$ in the HIT region 2. The passive scalar concentration is matched through a rapid transition layer as

$$Z(x,y) = f(x)^{\frac{1}{5}} \omega_1(x,y), \quad (8)$$

where f is introduced in relation (4).

The governing equation for the evolution of an incompressible two-dimensional temporal shearless mixing layer may be best expressed in terms of vorticity-stream function formulation:

$$\begin{aligned} \partial_t \omega + \nabla.(\mathbf{u}\omega) &= \frac{1}{\text{Re}} \nabla^2 \omega, \\ \omega &= -\nabla^2 \psi, \\ \mathbf{u} &= \nabla \times (\psi \widehat{e}_z), \end{aligned} \quad (9)$$

TABLE I. The specification of different initial conditions.

HIT region	Re_λ	Re_ℓ	L/ℓ	η/ℓ_1
1	180	90	200	0.1
2	8.2–731.7	4.11–360	50–800	0.052–0.48

where $\mathbf{u}$ is the incompressible velocity field, ω is the vorticity field, ψ is the stream function, and Re is the Reynolds number. The flow field also consists of the passive scalar $Z \in [0,1]$, governed by the following equation:

$$\partial_t Z + \mathbf{u} \cdot \nabla Z = \frac{1}{\text{RePr}} \nabla^2 Z, \quad (10)$$

where Pr is the Prandtl number. Given the reference values of velocity u_{ref}, length L_{ref}, constant density ρ, and constant thermodynamic properties, i.e., dynamic viscosity μ, mass specific heat c_p, and thermal conductivity κ, the Reynolds and Prandtl numbers may be, respectively, defined as

$$\text{Re} = \frac{\rho u_{\text{ref}} L_{\text{ref}}}{\mu}, \quad \text{Pr} = \frac{\mu c_p}{\kappa}. \quad (11)$$

Using appropriate reference values for ρ, μ, c_p, and κ, the Prandtl number is set as $\text{Pr} = 1$. Reference values u_{ref} and L_{ref} are considered as the square root of the turbulent kinetic energy and the length scale of HIT field 1, i.e., $\sqrt{E_1}$ and ℓ_1. Using these reference values the initial Reynolds number of the HIT field 1 is $\text{Re}_1 = 90$ while the initial Reynolds number for the HIT region 2 varies as $4.11 \leqslant \text{Re}_2 \leqslant 360$.

A summary of initial condition specifications, used in the numerical experiments, is listed in Table I. In this table, Re_λ is the Reynolds number defined based on the Taylor length scale $\lambda^2 = (E/\overline{u_x^2})$ and η is the Kolmogorov micro length scale.

Figure 3 provides further information about the initial turbulent fields by demonstrating the normalized energy spectra of three HIT fields. In this figure, the spectrum with the smallest spectral extent is related to the HIT region 2 with the lowest Reynolds number, i.e., $\text{Re}_2 = 4.11$. This energy spectrum and its subsequent flow field evolution correspond to a turbulent field in its final period of decay (see Ref. [33]). On the other hand, the spectrum with the widest spectral

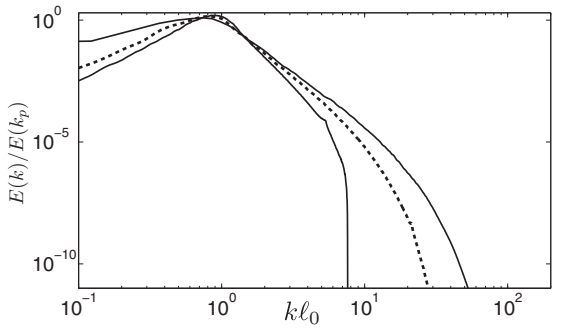

FIG. 3. The normalized energy spectra for different initial conditions. The spectrum with the shortest, middle, and largest spectral extents represent HIT flow fields with $\text{Re} = 4.11, 90$, and 360, respectively.

extent presents the HIT region 2 with the highest Reynolds number, i.e., $\mathrm{Re}_2 = 360$. The spectra of all other initial fields are located within the spectral envelope which is established by these two limiting high- and low-Reynolds-number spectra. In this figure, the normalized energy spectra of the HIT region 1, i.e., $\mathrm{Re}_1 = 90$, can also be seen between two high- and low-Reynolds-number spectra.

The two-dimensional computational domain is a square with periodic boundary conditions of period 2π in both space directions x and y. DNS experiments are performed using a classical pseudospectral method at the N^2 equally spaced (collocation) points, $N = 2048$. The nonlinear terms are calculated in physical space and dealiased using the 2/3 rule [37].

The time integration is performed using a low-storage, four-stage, fourth-order Runge-Kutta method with the coefficients of $\alpha_i = \{1/4, 1/3, 1/2, 1\}$. Variable time step Δt is used based on the Courant-Friedrichs—Lewy (CFL) condition:

$$\Delta t = \mathrm{CFL}\frac{\Delta x}{\sqrt{E_{\max}}}, \tag{12}$$

where $\mathrm{CFL} = 1.6$, Δx is the grid spacing, and $E_{\max}$ indicates the maximum value of the turbulent kinetic energy, over all the grid points. The total dimensionless integration time for all simulations is $\tau = 25$, beyond which the periodic boundary conditions can have an unphysical impact on the dynamics of the mixing layer.

B. gPC expansion

Following Wiener's homogeneous chaos theory, the best l^2-norm approximation of any random field $F(x,t;\boldsymbol{\chi})$ with finite variance can be expressed as a truncated expansion in terms of gPC [28,30,38],

$$F(\mathbf{x},t;\boldsymbol{\chi}) \approx \sum_{|\mathbf{i}|=0}^{M} a_{\mathbf{i}}(\mathbf{x},t)\Phi_{\mathbf{i}}(\boldsymbol{\chi}), \tag{13}$$

where $\boldsymbol{\chi} = \{\chi_1, \ldots, \chi_d\}$ is a random vector with mutually independent and identically distributed (IID) random components χ_i, $a_{\mathbf{i}}(\mathbf{x},t)$ are deterministic modal coefficients, and $\mathbf{i} = (i_1, \ldots, i_d)$ is the multi-index with $\mathbf{i} = i_1 + \cdots + i_d$ [39]. The expansion basis $\Phi_{\mathbf{i}}(\boldsymbol{\chi})$ are the d-dimensional **i**th-degree gPC which can be expressed as the products of the corresponding one-dimensional gPC polynomials

$$\Phi_{\mathbf{i}}(\boldsymbol{\chi}) = \sum_{\mathbf{i}=i_1+\cdots+i_d} \phi_{i_1}(\chi_1)\cdots\phi_{i_d}(\chi_d), \tag{14}$$

where summation is over all combinations of the products in which $\mathbf{i} = i_1 + \cdots + i_d$. The basis function $\phi_{i_m}(\chi_m)$ is the one-dimensional i_mth-degree gPC in the direction parameterized by random variable χ_m with following orthogonality relation:

$$\langle \phi_i(\chi_d)\phi_j(\chi_d)\rangle = \langle \phi_i^2\rangle \delta_{ij}. \tag{15}$$

In relation (15), δ_{ij} is the delta function and $\langle\rangle$ denotes the ensemble average expressed as an inner product,

$$\langle f(\chi)g(\chi)\rangle = \int f(\chi)g(\chi)\mathrm{PDF}(\chi)d\chi, \tag{16}$$

where $\mathrm{PDF}(\chi)$ is the probability density function of IID random variables χ_i. Following relations (14)–(16), expansion basis $\Phi_{\mathbf{i}}(\boldsymbol{\chi})$ are orthogonal polynomials with respect to a weight function which corresponds to the PDF of the random variables χ_i. Therefore, polynomial basis in expansion (13) has to be chosen based on the correspondence between the weighting function of the orthogonal polynomial family and the PDF of the random variables χ_i.

In this research, random variables χ_i control the initial condition parameters $\mathscr{L}$ and $\mathscr{E}$, which are considered as uniformly distributed random variables with bounded supports. This choice for their PDF does not favor any particular turbulent flow and generalizes the results of the sensitivity analysis. Therefore, the orthogonal basis in expansion (13) has to be constructed based on the Legendre polynomials, which its orthogonality weight function is consistent with uniform distribution [29].

In a nonintrusive approach [32], the gPC modal coefficients $a_{\mathbf{i}}(\mathbf{x},t)$ in expansion (13) are computed by projecting the random field $F(\mathbf{x},t;\boldsymbol{\chi})$ onto orthogonal multivariate gPC basis $\Phi_{\mathbf{i}}(\boldsymbol{\chi})$,

$$a_{\mathbf{i}}(\mathbf{x},t) = \frac{\langle F(\mathbf{x},t;\boldsymbol{\chi}).\Phi_{\mathbf{i}}(\boldsymbol{\chi})\rangle}{\langle \Phi_{\mathbf{i}}^2\rangle}. \tag{17}$$

The inner product in the numerator of (17) involves multi-dimensional numerical integration, which, using appropriate indexing, can be concisely expressed as

$$\langle F(\mathbf{x},t;\boldsymbol{\chi})\cdot\Phi_{\mathbf{i}}(\boldsymbol{\chi})\rangle \approx \sum_{\mathbf{j}=0}^{N_q} F(\boldsymbol{\chi}^{(\mathbf{j})})\Phi_{\mathbf{i}}(\boldsymbol{\chi}^{(\mathbf{j})})\boldsymbol{w}_{\mathbf{i}}^{(\mathbf{j})}, \tag{18}$$

where for the sake of brevity the dependency of F on $\mathbf{x}$ and t is omitted in summation. The index $\mathbf{j}$ and $\boldsymbol{w}_{\mathbf{i}}^{(\mathbf{j})}$ refer to the nodes and integration weights of the N_q quadrature points. Based on the numerical integration theory, for optimal accuracy, the quadrature points $\boldsymbol{\chi}^{(\mathbf{j})}$ must be the roots of the polynomials Φ. Choosing the type of the gPC basis function, which in this research is the Legendre polynomial, these specific points have to be roots of these polynomials, including the boundary nodes which are known as Legendre-Gauss-Lobatto (LGL) quadrature points [40].

Using explicit Eq. (13), a large population of solutions can be reconstructed at the expense of algebraic evaluation instead of conducting DNS. From this large population of solutions, it is also possible to construct interpolate response surfaces for different flow field quantities in sample space $\mathscr{L}$-$\mathscr{E}$. These response surfaces provide visual information about the sensitive dependence of the physical quantities under consideration on the controlling random variables. Moreover, statistical moments and the PDF of the solution can be also easily extracted from this large population of solutions.

The sensitivity analysis of the system can be also carried out by decomposing the variance of $F(x,t;\boldsymbol{\chi})$ into fractions which originate from variations of different random arguments χ_i, using Sobol's sensitivity index [41],

$$D_i = \frac{\mathrm{var}\{F(x,t;\boldsymbol{\chi})|\chi_i\}}{\sigma_F^2}, \tag{19}$$

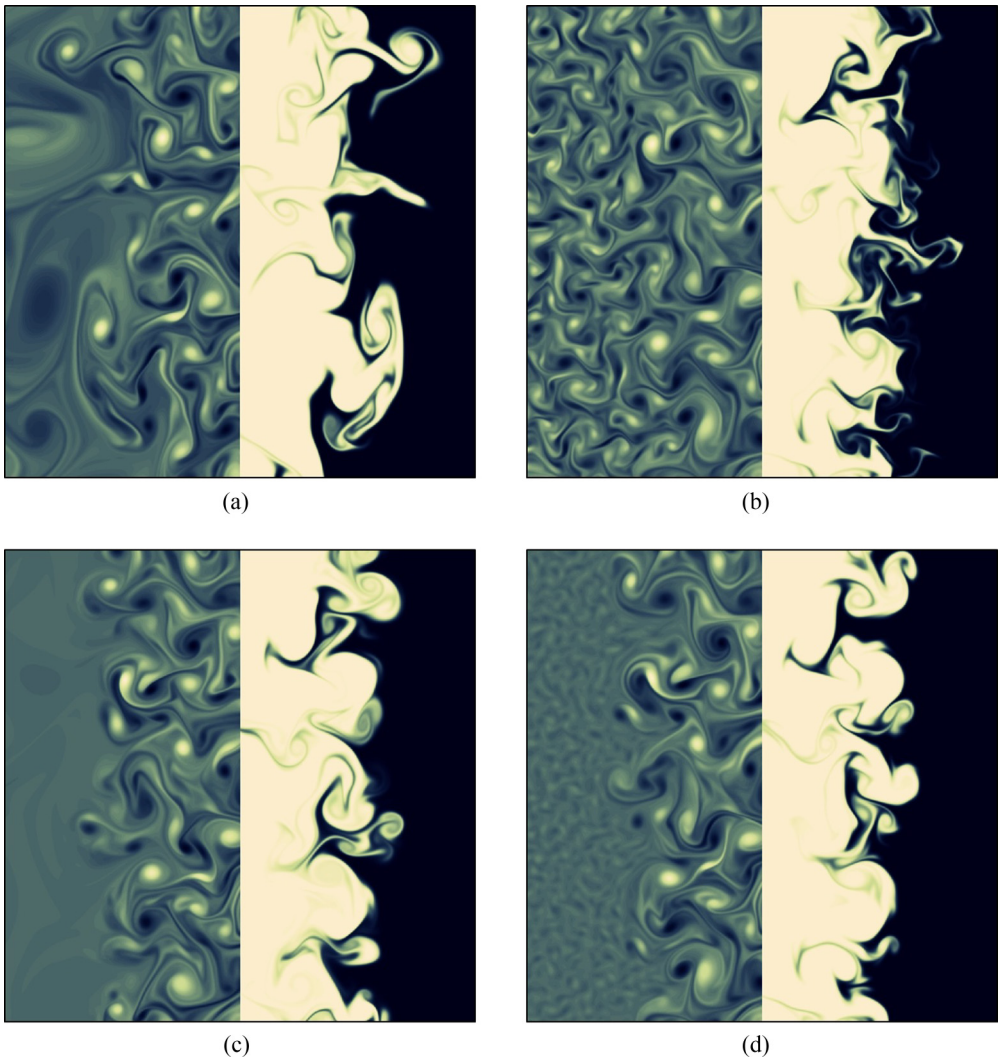

FIG. 4. Vorticity-scalar snapshots of shearless mixing layers with four different imposed $\mathscr{E}$ and $\mathscr{L}$ at $\tau = 20$. In each snapshot, the scalar field is located at the right part of the plane (presented in bright-black color) and the vorticity field is located at the left part of the plane (presented in gray). The horizontal and vertical axes are, respectively, the inhomogeneous and the homogeneous directions. (a) $\mathscr{L} = 1/4, \mathscr{E} = 1$; (b) $\mathscr{L} = 4, \mathscr{E} = 1$; (c) $\mathscr{L} = 1/4, \mathscr{E} = 30$; (d) $\mathscr{L} = 4, \mathscr{E} = 30$.

where the numerator represents the variation of F originated from variation of χ_i and denominator is the total variance of F. Similarly, the combined effects of the variations of different χ_i on the variability of $F(x,t;\boldsymbol{\chi})$ can be obtained based on the higher-order sensitivity indices:

$$D_{i_1 \cdots i_m} = \frac{\mathrm{var}\left\{F(x,t;\boldsymbol{\chi})|\chi_{i_1} \cdots \chi_{i_m}\right\}}{\sigma_F^2}. \tag{20}$$

Correspondingly, the numerator represents the variation of F originated from interactions among $\chi_{i_1} \cdots \chi_{i_m}$.

Since in this research two controlling parameters $\mathscr{E}$ and $\mathscr{L}$ are considered, the variance of any flow field quantity can be decomposed into three parts, D_E, D_L, and $D_{E,L}$. Sobol's indices D_E and D_L respectively represent fractions of the flow field variance which are caused by variations of $\mathscr{E}$ and $\mathscr{L}$. Moreover, due to the nonlinear nature of the flow field evolution, the impact of variation of $\mathscr{E}$ (or $\mathscr{L}$) on the flow field variance can be modified by varying $\mathscr{L}$ (or $\mathscr{E}$). The mixed index $D_{E,L}$ measures the fraction of the flow field variance, which originates from this interaction between $\mathscr{E}$ and $\mathscr{L}$.

III. RESULTS

The overall evolution of a shearless mixing layer may be described as follows. Due to the random motions of the coherent vortical structures in two adjacent HIT fields, eddies with large kinetic energies intermittently penetrate from one HIT field into the other HIT field. As a result of these penetrations, a layer between these two adjacent HIT fields is formed in which velocity statistics are non-Gaussian and highly intermittent.

Figure 4 visualizes four different vorticity ω and scalar concentration Z fields at $\tau = 20$, corresponding to four extremum values of the initial condition parameters $\mathscr{E}$ and $\mathscr{L}$. In each snapshot the vorticity field ω is presented in gray at the left part of the plane and the scalar concentration Z is in black at the right part of the plane. The penetrations of vortical

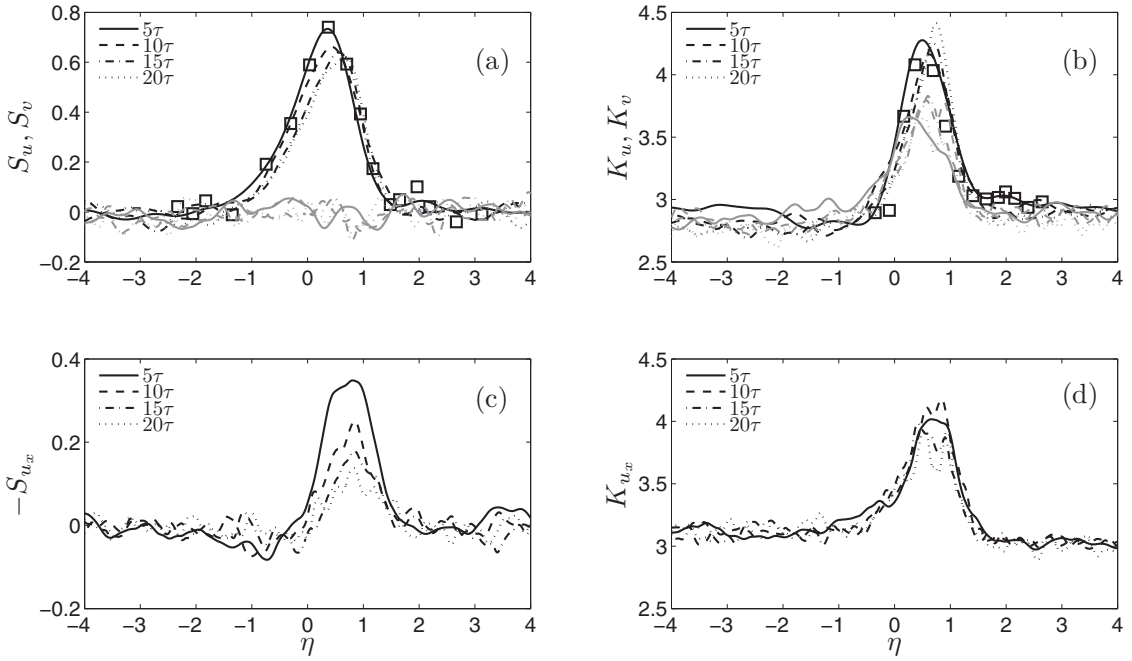

FIG. 5. Spatial distribution of the velocity skewness and kurtosis for the mixing layer with $\mathscr{E} = 6.7$ and $\mathscr{L} = 1.0$. The HIT regions 1 and 2 are respectively located at $\eta < 0$ and $\eta > 0$ where $\eta = x/\Delta$ is the inhomogeneous coordinate x normalized by the mixing layer width Δ. [(a) and (b)] Skewness and kurtosis of the velocity components in inhomogeneous and homogeneous directions, i.e., u and v, at different times. Darker curves represent u; gray curves represent v; symbols □ represent data from Ref. [23]. [(c) and (d)] Skewness and kurtosis of the velocity derivative $\partial u/\partial x$ at different times. Note that to provide a direct comparison between skewnesses of velocity and velocity derivative, $-S_{u_x}$ is plotted in (c).

structures from one HIT region into the adjacent HIT region deforms the scalar interface structure and creates different fluid regions [19]: intermittent regions of coherent vortical structures, regions with a stretched interface in which fluid packets are engulfed, and regions with intricate and corrugated small-scale structures.

Variations of the initial condition parameters $\mathscr{E}$ and $\mathscr{L}$ can reshape these different regions and, consequently, the statistical character of the mixing region. By comparing Figs. 4(a) and 4(d), it can be seen that increasing $\mathscr{E}$ and $\mathscr{L}$ leads to more frequent penetration of the coherent vortical structures into the mixing region and more intermittent formation of the engulfment regions. The impact of $\mathscr{E}$ and $\mathscr{L}$ on the mixing layer intermittency and deviation from Gaussianity is studied in detail in Sec. III A.

Moreover, by comparing Figs. 4(b) and 4(c), it can be observed that increasing $\mathscr{L}$ and total turbulent kinetic energy (which in this case is equivalent to reduction of $\mathscr{E}$) leads to exceeding formation of the intricate and tangled small-scale structures, in which small-scale mixing occurs. In Sec. III C impact of $\mathscr{L}$ and total turbulent kinetic energy on the flow filed mixing efficiency is investigated.

In the following results, for any flow field quantity $\tilde{\phi}$, the uppercase letter Φ denotes the mean quantity and the lowercase letter ϕ represents the fluctuation part, i.e., $\tilde{\phi} = \Phi + \phi$. To obtain reasonable and repeatable statistical results for any sample solution $\tilde{\phi}$, at each $N_q = 121$ quadrature node, 200 independent and statistically identical realizations are generated by performing DNS. The variability of the flow field quantity $\tilde{\phi}$ is examined by generating 10^6 random sample solutions using explicit form of the corresponding 10th-order truncated gPC polynomials.

A. Intermittency and anisotropy

The skewness and kurtosis of the velocity component u_i are respectively defined as

$$S_{u_i} \equiv \frac{\overline{u_i^3}}{\left(\overline{u_i^2}\right)^{3/2}}, \qquad K_{u_i} \equiv \frac{\overline{u_i^4}}{\left(\overline{u_i^2}\right)^2}, \tag{21}$$

where $u_1 = u$ and $u_2 = v$ are the inhomogeneous and homogeneous components of the velocity field $\mathbf{u}$. Using these quantities, intermittency and departure from Gaussianity inside the mixing layer, caused by the intermittent penetration of energetic eddies, can be measured.

It should be noted that intermittency implies non-Gaussianity but not necessarily vice versa. The kurtosis of any variable which is a nonlinear function of a Gaussian flow field may show deviation from a Gaussian value 3. Similarly, passive scalars can also show nonzero odd moments, which does not reflect intermittency aspects of the flow field dynamics. However, skewness and kurtosis of the velocity field and its derivative may be appropriate indicators of intermittency [42, ch. 7].

Figure 5 shows velocity skewness and kurtosis at different times for a mixing layer with $\mathscr{E} = 6.7$ and $\mathscr{L} = 1.0$, similar to the performed numerical experiment by Tordella and Iovieno on a three-dimensional mixing layer [23]. In this figure, HIT regions 1 and 2 are respectively located at $\eta < 0$ and

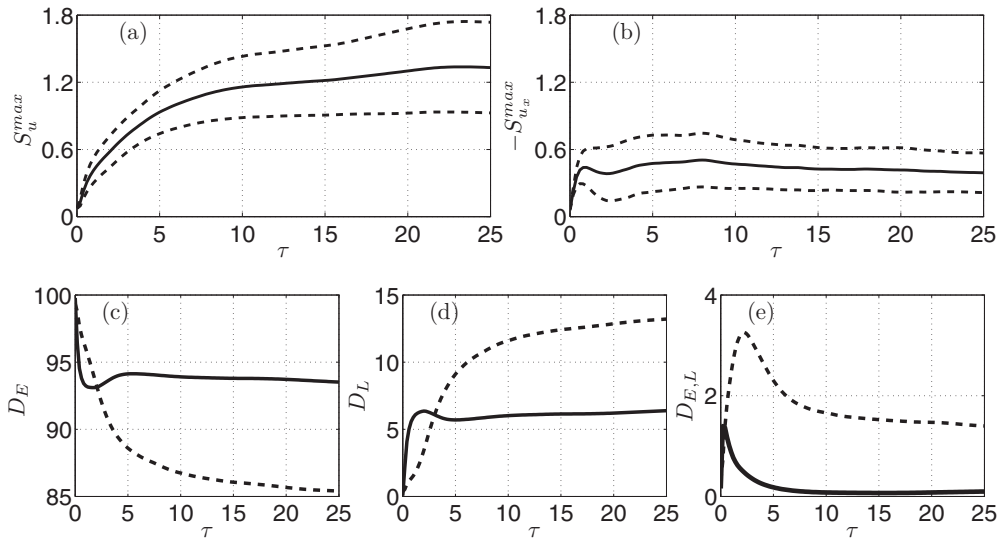

FIG. 6. Time evolutions of mean solutions and standard deviation envelopes of (a) $S_u^{\max}$ and (b) $-S_{u_x}^{\max}$; (—) mean solution; (− − −) mean ± STD. Time evolutions of the Sobol's sensitivity indices with respect to the variations of (c) energy ratio, (d) integral length scale ratio, and (e) interaction of their covariation; (—) sensitivity index of $S_u^{\max}$; (− − −) sensitivity index of $S_{u_x}^{\max}$.

$\eta > 0$ where $\eta = x/\Delta$ is the inhomogeneous coordinate x normalized by the mixing layer width Δ. The width Δ is equal to the distance between the points with scalar $0.25 \leqslant Z(\mathbf{x},t) \leqslant 0.75$.

From Fig. 5(a), it can be clearly observed that in HIT regions 1 and 2 both S_u and S_v show the Gaussian value of zero. Within the mixing layer the inhomogeneous velocity component skewness S_u takes a positive value, which indicates intermittent motions of energetic eddies across the mixing layer from HIT region 1 toward HIT region 2. Statistical invariance of the velocity field under the reflection of the homogeneous axis y yields an even function for the PDF of v and, consequently, zero S_v inside the mixing region (see Ref. [43], p. 89).

As a further indication of the intermittency and departure from Gaussianity, the kurtosis of the inhomogeneous and homogeneous velocity components, i.e., K_u and K_v, are shown in Fig. 5 (b). Kurtosis of both velocity components u and v remains close to the Gaussian value $K = 3$ in HIT regions and show significant deviation from the Gaussianity inside the mixing layer. However, comparing maximum values of K_u and K_v reveals that the inhomogeneous velocity component, u, is more intermittent than the homogeneous velocity component v.

In Figs. 5(a) and 5(b) a close agreement between numerical experiment of the three-dimensional mixing layer, indicated by square symbols, and the current two-dimensional mixing layer can be observed [23]. It may be concluded that motions of energetic eddies inside the mixing region result in identical intermittency and departure from the Gaussianity in two- and three-dimensional flow field evolutions.

Likewise, Gaussian departure of the small scale structures and their intermittency can be analyzed by the skewness and kurtosis of the velocity derivative. Indeed intermittency of the small scales, embodied in velocity derivative skewness, has a significant effect on the turbulent flow field evolution: in a three-dimension field it is responsible for the enstrophy production while in the two-dimensional field it leads to the palinstrophy production [34].

Figures 5(c) and 5(d) show the spatial distribution of the $S_{u_x} \equiv \overline{(\partial u/\partial x)^3}/[\overline{(\partial u/\partial x)^2}]^{3/2}$ and $K_{u_x} \equiv \overline{(\partial u/\partial x)^4}/[\overline{(\partial u/\partial x)^2}]^2$. It can be seen that both quantities increased beyond the isotropic turbulence value within the mixing layer. The noticeable feature is that the maxima of $-S_{u_x}$ and K_{u_x} are lower than the maxima of S_u and K_u, which implies that large scales are more intermittent than small scales. This higher level of the intermittency of large scales can be attributed to the inverse energy cascade in two-dimensional turbulence. Indeed, the flow of energy from small scales toward large scales regularizes the small scale dynamics close to quasi-Gaussian and nonintermittent statistical properties [44].

To investigate the impact of the variations of $\mathscr{E}$ and $\mathscr{L}$ on the variabilities of the flow field intermittency, time evolutions of maximum values of S_u and S_{u_x}, i.e., $S_u^{\max}$ and $S_{u_x}^{\max}$, are reconstructed using gPC polynomials. In Fig. 6, reconstructed mean solutions and standard deviation envelopes of $S_u^{\max}$ and $S_{u_x}^{\max}$ are reported. The standard deviation envelope consists in adding and subtracting one standard deviation unit from the mean value and spans a 33% confidence interval for an identically distributed population.

In Figs. 6(a) and 6(b), both $S_u^{\max}$ and $S_{u_x}^{\max}$ start to increase from an almost initial isotropic statistic. On average, $S_u^{\max}$ shows a monotonic increase with time while $S_{u_x}^{\max}$ develops to an almost temporal asymptotic value $\sim(0.42 \pm 0.2)$. The wider variance envelop of $S_u^{\max}$ compared to that of $S_{u_x}^{\max}$ clearly shows that the intermittency of large scales is more sensitive to the variations of $\mathscr{E}$ and $\mathscr{L}$ compared to the small-scale intermittency. Therefore, in two-dimensional turbulence, smaller structures show lower levels of intermittency and less sensitivity to the initial condition parameters compared to the larger-scale structures. Sensitivities of the large- and small-scale intermittencies to the variations of $\mathscr{E}$ and $\mathscr{L}$ can be further examined by decomposing total variances of $S_u^{\max}$

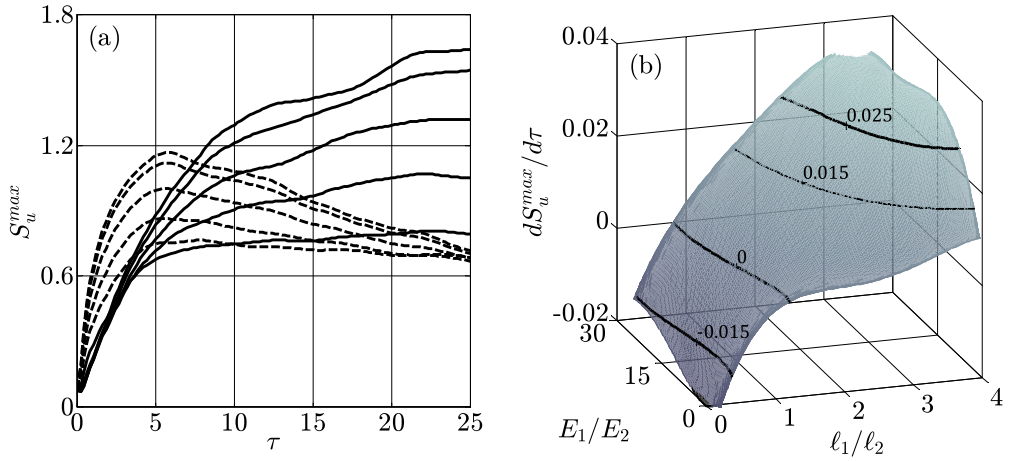

FIG. 7. Maximum skewness of the inhomogeneous velocity component $S_u^{\max}$. (a) Time evolutions of $S_u^{\max}$ for mixing layers with $\mathscr{E} = 6.7$ and different $\mathscr{L}$s. Mixing layers with $\mathscr{L} < 1.0$ (− − −) and $\mathscr{L} > 1.0$ (——) show moderate reduction and monotonic increase in $S_u^{\max}$ at the well-developed stage $\tau \geqslant 10$, respectively . (b) Response surface of the maximum skewness growth rate, $dS_u^{\max}/d\tau$, as a function of $\mathscr{E}$ and $\mathscr{L}$.

and $S_{u_x}^{\max}$ into the three parts, D_E, D_L, and $D_{E,L}$, using Sobol's sensitivity index. Graphically, D_E and D_L indicate fractions of the standard deviation envelopes area which originate from the variations of $\mathscr{E}$ and $\mathscr{L}$ respectively. The mixed Sobol's index $D_{E,L}$ measures the fraction of the standard deviation envelope area which originates from interactions between $\mathscr{E}$ and $\mathscr{L}$.

Figure 6(c) shows that more than 85% of contributions to the large- and small-scale intermittency comes from variations of $\mathscr{E}$ while the contribution from variations of $\mathscr{L}$ is at most 15% [in Fig. 6(b)]. Figure 6(c) shows that interaction of $\mathscr{E}$ and $\mathscr{L}$ has a negligible influence on the total variances of $S_u^{\max}$ and $S_{u_x}^{\max}$, i.e., less than 5%. Therefore, the most influential parameters on the intermittency is $\mathscr{E}$ while $\mathscr{L}$ has a secondary effect on the flow field intermittency. Velocity kurtosis K_u and K_{u_x} show completely similar behavior for intermittency, which are not shown.

Impacts of $\mathscr{E}$ and $\mathscr{L}$ on the development of the mixing layer intermittency is further investigated in Fig. 7, which presents the time evolution of $S_u^{\max}$. In Fig. 7(a) time evolutions of $S_u^{\max}$ for mixing layers with identical $\mathscr{E} = 6.7$ and different $\mathscr{L}$s are shown. It can be observed that during the flow field evolution in the well-developed stage, i.e., $\tau \geqslant 10$, mixing layers with $\mathscr{L} < 1.0$ show a moderate reduction in $S_u^{\max}$ while for $\mathscr{L} > 1.0$ this quantity undergoes a monotonic increase.

This issue is further established in Fig. 7(b) by demonstrating $dS_u^{\max}/d\tau$ as a function of $\mathscr{E}$ and $\mathscr{L}$. The response surface is constructed based on the average of $dS_u^{\max}/d\tau$ over $10 \leqslant \tau \leqslant 25$. First, it can be observed that the growth rate of the intermittency, presented by $dS_u^{\max}/d\tau$, is a monotonic function of both $\mathscr{E}$ and $\mathscr{L}$. Second, it can be seen that for the mixing layer with $\mathscr{L} > 1.0$ the mixing region becomes increasingly intermittent as the flow field evolves, i.e., $dS_u^{\max}/d\tau > 0$, while for the imposed $\mathscr{L} < 1.0$ the intermittency annihilates during the well-developed stage of the flow field evolution, i.e., $dS_u^{\max}/d\tau < 0$. The borderline for these bifurcation is the contour line $\mathscr{L} = 1.0$.

Considering the monotonic dependence of $dS_u^{\max}/d\tau$ on $\mathscr{E}$ and the dominant effect of the later parameter on the evolution of $S_u^{\max}$, this behavior can be related to the effective turbulent kinetic energy ratio of two interacting HIT regions, i.e., $E_1(\tau)/E_2(\tau)$. For a mixing layer with imposed $\mathscr{L} < 1.0$, i.e., $\ell_1 < \ell_2$, the HIT region 1 has a higher turbulent kinetic energy decay rate than that in HIT region 2. Therefore, during the flow field evolution the effective turbulent kinetic energy ratio of two interacting HIT regions decreases. The situation for the concordant imposed $E_1 > E_2$ and $\ell_1 > \ell_2$ is the opposite: The higher turbulent kinetic energy decay rate of the HIT region 2 than that in HIT region 1 amplifies the effective turbulent kinetic energy ratio of the two interacting HIT regions during the flow field evolution

As another intermittency characteristic, the penetration depth of the energetic eddies can be considered, which is defined as the averaged locations of the maxima of skewness, x_s, and kurtosis x_k, i.e., $x_{\max} = (x_s + x_k)/2$. It is found that after few turn over eddy times, the normalized penetration depth $\eta_{\max} = x_{\max}/\Delta$ achieves an asymptotic value, which is reported in Fig. 8. Figure 8(a) shows $\eta_{\max}$ as a function of $\mathscr{E}$ and $\mathscr{L}$. Similarly to the intermittency growth rate $dS_u^{\max}/d\tau$, the penetration depth $\eta_{\max}$ is also a monotonic function of both $\mathscr{E}$ and $\mathscr{L}$. The response surface shows a sharp increase for $\mathscr{E} \leqslant 10$ and afterward bends to a plateau, which implies that in this region the penetration depth is less sensitive to the variations of $\mathscr{E}$ and $\mathscr{L}$ in comparison to the region with a sharp increase.

As discussed above, the evolution of a mixing layer with imposed $\mathscr{L} < 1$ is accompanied by the reduction of turbulent kinetic energies ratio of the two interacting HIT regions, i.e., $E_1(\tau)/E_2(\tau)$. Since the overall tendency of intermittent turbulent penetration is from the high-energy HIT region toward the low-energy HIT region [8,23], the penetration of energetic eddies are suppressed when $\mathscr{L} < 1$. This issue can be clearly seen from the negative value of the penetration depth in regions with $\mathscr{E} = 1$ and $\mathscr{L} < 1$, which indicates that the motions of the energetic eddies are from HIT region 2 toward the HIT region 1.

This visual information from the response surface is closely related to the PDF of $\eta_{\max}$, presented in Fig. 8(b). The

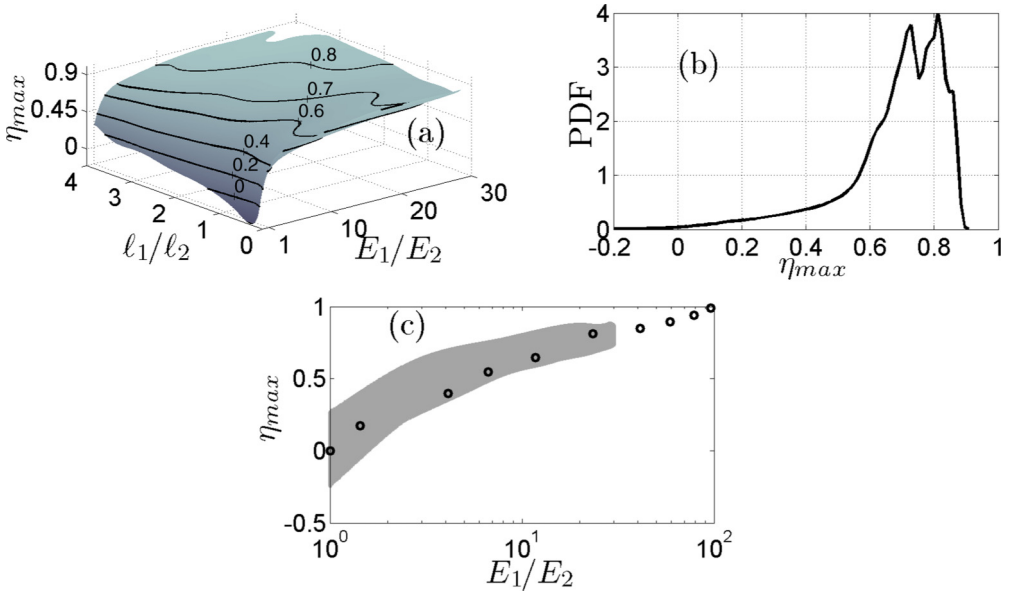

FIG. 8. Normalized position of the maximum skewness $\eta_{\max} = x_{\max}/\Delta$. (a) Response surface of $\eta_{\max}$ as a function of $\mathscr{E}$ and $\mathscr{L}$. (b) PDF of $\eta_{\max}$. (c) $\eta_{\max}$ as a function of $\mathscr{E}$. The gray region represents 10^6 sample data with uncertainty of initial integral length scales, $\mathscr{L}$. Symbols in (c) represent DNS data of Ref. [45].

concentrated peak in the PDF distribution in Fig. 8(b), i.e., $0.6 \leqslant \eta_{\max} \leqslant 0.9$, is the most probable penetration depth and corresponds to the plateau region of the response surface. In contrast, the wide spread tail of the PDF distribution, i.e., $\eta_{\max} \leqslant 0.5$, originates from large variations of $\eta_{\max}$ and corresponds to the large gradient regions of the response surface.

Finally, Fig. 8(c) shows the envelop of penetration depths generated by varying $\mathscr{E}$ and $\mathscr{L}$. The width of the envelope at constant $\mathscr{E}$ represents the impact of $\mathscr{L}$ on the variability of $\eta_{\max}$. The monotonic dependence of $\eta_{\max}$ on $\mathscr{E}$ can be clearly observed in this figure. Moreover, the width of the envelope decreases by increasing $\mathscr{E}$, which means that at higher energy ratios the penetration depth shows less sensitivity to the variations of $\mathscr{L}$. For the sake of comparison, in this figure the penetration depths of a three-dimensional mixing layer are also included by symbols which fall within the solution envelope [45].

In Fig. 9, correlations among pertinent intermittency measures are investigated. In Fig. 9(a), maxima of skewness and kurtosis of the inhomogeneous velocity components from all simulations at different times are plotted against each other. It can be seen that individual values follow an almost quadratic relation $K_u^{\max} = 3 + 2.615(S_u^{\max})^{1.75}$ in the S_u-K_u plane. Notably, Tordella and Iovieno [26] reported a quite similar scaling relation, namely $K_u^{\max} = 3 + 2.5(S_u^{\max})^2$, from their numerical experiment of a three-dimensional mixing layer. This close analogy, however, indicates that the dynamics of energetic eddies in two- and three-dimensional flow field evolutions have similar intermittent characters.

In Fig. 9(a), the borderline of the Betchov [46] inequality, i.e., $(21/4)S^2 \leqslant K$, is also included by the dashed line, which clearly shows that the relation between $S_u^{\max}$ and $K_u^{\max}$ violates the Betchov inequality in some regions with a high level of intermittency. It should be noted that this inequality exists between the fluid velocity dkewness and kurtosis at identical spatiotemporal coordinate while locations of the maxima of skewness, x_s, and kurtosis, x_k, are not identical.

In Fig. 9(b) the maxima of the velocity components of kurtosis, i.e., $K_u^{\max}$ and $K_v^{\max}$, from all simulations at different times are plotted against each other. From the linear correlation between $K_u^{\max}$ and $K_v^{\max}$ one might conclude that the main part of the homogeneous fluctuations, v, in mixing layer is directly originated from the inhomogeneous velocity fluctuations, u. Indeed, as energetic eddies penetrate into the mixing layer, during their evolution some part of the inhomogeneous velocity fluctuations, u, is transferred into the homogeneous component, v, via the pressure-velocity correlations. However, penetrating eddies with relatively low kinetic energies will decay before this directional energy transfer can be accomplished, which results in a lower value of $K_v^{\max}$ compared to $K_u^{\max}$.

B. Transport equations for statistical moments and kinetic energy

To further investigate the two-dimensional shearless mixing layer evolution, dynamics of $\overline{u^2}$, $\overline{u^3}$, $\overline{u^4}$ and turbulent kinetic energy $E = (\overline{u^2} + \overline{v^2})/2$ are discussed in this section. Dynamic equations for the velocity second-order moments, i.e., $\overline{u^2}$ and $\overline{v^2}$, may be written as

$$\frac{\partial \overline{u^2}}{\partial t} + \underbrace{\frac{\partial}{\partial x}\left(\overline{u^3} + 2\overline{pu} - \nu\frac{\partial \overline{u^2}}{\partial x}\right)}_{\text{Transport}} = \underbrace{2\left(\overline{p\frac{\partial u}{\partial x}}\right)}_{\text{Redistribution}} - \underbrace{2\nu\left(\overline{\left(\frac{\partial u}{\partial x}\right)^2 + \left(\frac{\partial u}{\partial y}\right)^2}\right)}_{\text{Dissipation}}, \tag{22}$$

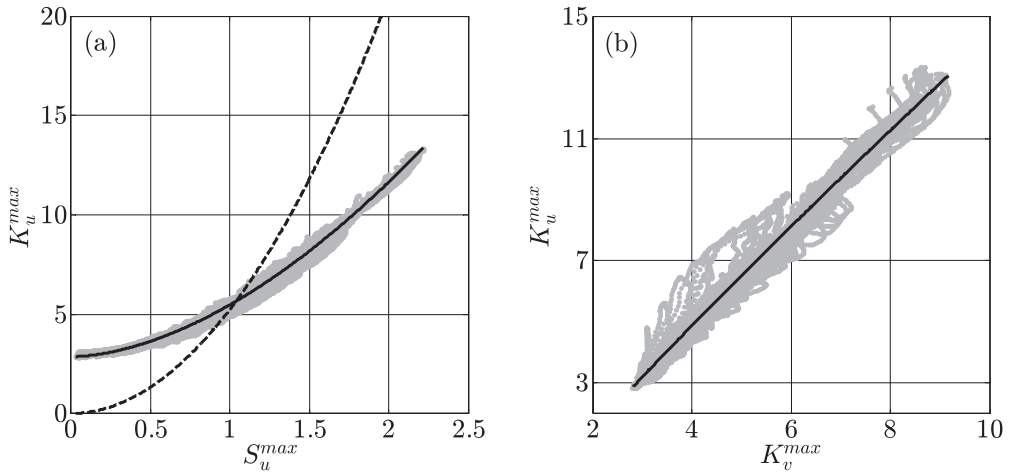

FIG. 9. (a) $K_u^{\max}$ as a function of $S_u^{\max}$. The line shows the scaling $K_u^{\max} = 3 + 2.615(S_u^{\max})^{1.75}$. The Betchov inequality $K \geqslant (21/4)S^2$ is also included by dash line. (b) $K_u^{\max}$ as a function of $K_v^{\max}$.

and

$$\frac{\partial \overline{v^2}}{\partial t} + \underbrace{\frac{\partial}{\partial x}\left(\overline{uv^2} - \nu\frac{\partial \overline{v^2}}{\partial x}\right)}_{\text{Transport}} = \underbrace{2\left(\overline{p\frac{\partial v}{\partial x}}\right)}_{\text{Redistribution}} - \underbrace{2\nu\overline{\left(\left(\frac{\partial v}{\partial x}\right)^2 + \left(\frac{\partial v}{\partial y}\right)^2\right)}}_{\text{Dissipation}}, \tag{23}$$

where in the above equations the constant density ρ is absorbed into the static pressure $\check{p}$, resulting in the modified pressure $p = \check{p}/\rho$. Moreover, ν is the constant kinematic viscosity, and x and y are, respectively, the inhomogeneous and homogeneous directions. Evolution of the turbulent kinetic energy E is obtained by combining Eqs. (22) and (23):

$$\frac{\partial E}{\partial t} + \underbrace{\frac{\partial}{\partial x}\left(\frac{\overline{u(u^2+v^2)}}{2} + \overline{pu} - \nu\frac{\partial E}{\partial x}\right)}_{\text{Transport}} = \underbrace{-\nu\overline{\left(\left(\frac{\partial u}{\partial x}\right)^2 + \left(\frac{\partial u}{\partial y}\right)^2 + \left(\frac{\partial v}{\partial x}\right)^2 + \left(\frac{\partial v}{\partial y}\right)^2\right)}}_{\text{Dissipation}}. \tag{24}$$

Similarly, governing equations for $\overline{u^3}$ and $\overline{u^4}$ can be written as follows:

$$\frac{\partial \overline{u^3}}{\partial t} + \underbrace{\frac{\partial}{\partial x}\left(\overline{u^4} - \frac{3}{2}(\overline{u^2})^2 + 3\overline{pu^2} - \nu\frac{\partial \overline{u^3}}{\partial x}\right)}_{\text{Transport}} = \underbrace{3\left(\overline{p\frac{\partial u^2}{\partial x}}\right)}_{\text{Redistribution}} - \underbrace{6\nu\overline{u\left(\frac{\partial u^2}{\partial x} + \frac{\partial u^2}{\partial y}\right)}}_{\text{Dissipation}}, \tag{25}$$

and

$$\frac{\partial \overline{u^4}}{\partial t} + \underbrace{\frac{\partial}{\partial x}\left(\overline{u^5} + 4\overline{u^3}\,\overline{u^2} + 4\overline{pu^3} - \nu\frac{\partial \overline{u^4}}{\partial x}\right)}_{\text{Transport}} = \underbrace{4\left(\overline{p\frac{\partial u^3}{\partial x}}\right)}_{\text{Redistribution}} - \underbrace{\overline{u^2}\frac{\partial \overline{u^3}}{\partial x}}_{\text{Production}} - \underbrace{12\nu\overline{u^2\left(\frac{\partial u^2}{\partial x} + \frac{\partial u^2}{\partial y}\right)}}_{\text{Dissipation}}. \tag{26}$$

Profiles of different terms of dynamics equations of $\overline{u^2}$, $\overline{u^3}$, $\overline{u^4}$, and E across the mixing layer with imposed $\mathscr{E} = 15.5$ and $\mathscr{L} = 2.125$ are shown in Figs. 10(a)–10(d). Besides ensemble averaging, these profiles are obtained by further time averaging over the time interval $10 \leqslant \tau \leqslant 25$, in which the peaks of profiles remain almost constant. The inhomogeneous coordinate has been mapped on the mixing layer width and is nondimensionalized by the mixing layer width, i.e., $\eta = x/\Delta$. Similarly to Fig. 5, HIT regions 1 and 2 are respectively located at $\eta < 0$ and $\eta > 0$. In Figs. 10(a)–10(d) different terms are plotted in such a way that their positive and negative values denote gain and loss of their respective quantities.

Transport terms are responsible for the spatial distribution of $\overline{u^2}$, $\overline{u^3}$, $\overline{u^4}$, and E throughout the mixing region by convecting them from the neighborhood of the high-energy HIT region 1 toward the low-energy HIT region 2. This issue can be observed in Figs. 10(a)–10(d), which show that transport terms take negative values in $\eta < 0$ while they are positive in $\eta > 0$. The effect of the transport terms on the total amount of the pertinent quantity inside the mixing layer is restricted to the net flux from the homogeneous regions 1 and 2. Transport terms for the even moments $\overline{u^2}$, $\overline{u^4}$, and E consist of odd moments and viscous transport terms, i.e., $\nu\partial_x(\bullet)$, which are zero in HIT regions 1 and 2. Therefore, for even-velocity moments the transport terms contribute to the spatial distribution inside the mixing layer without altering the total amount. The net flux of the transport term of the odd moment $\overline{u^3}$ can be analyzed by means of simplifying

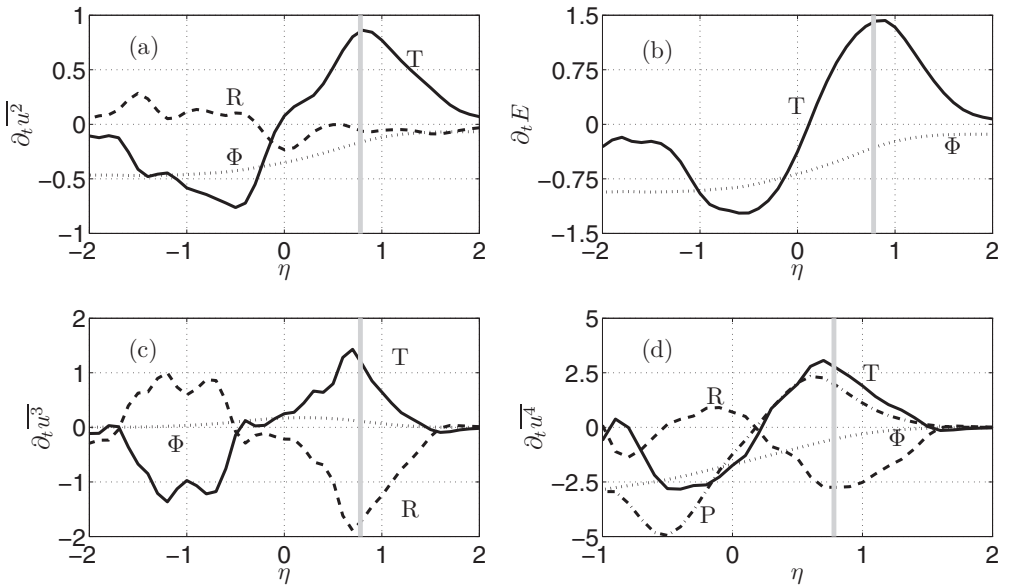

FIG. 10. Statistical moment budget terms cross the mixing layer with imposed $\mathscr{E} = 15.5$ and $\mathscr{L} = 2.125$. The HIT region 1 is at $\eta < 0$ and position of maximum intermittency is indicated by vertical gray line. Terms of transport equations of (a) $\overline{u^2}$, (b) E, (c) $\overline{u^3}$, and (d) $\overline{u^4}$. For the sake of clarity, the highly oscillatory behavior of $\overline{u^4}$ in $-2 < \eta < -1$ is not shown. (—) Transport term (T); (- - -) redistribution term (R);(-.-.-) production term (P); (...) dissipation term (Φ).

hypotheses: (i) the pressure transport is almost proportional to the convective transport associated to the fluctuations, i.e., $\overline{pu^2} \sim \overline{u^4}$; (ii) neglecting the viscose transport term; and (iii) considering Gaussian distribution in HIT regions, i.e., $\overline{u^4} = 3\overline{u^2}$. Using these assumptions, the transport term of $\overline{u^3}$ may be considered proportional to the difference of the turbulent kinetic energies of HIT regions 1 and 2, i.e., $[E_1(t) - E_2(t)]/\Delta(t)$.

As can be observed in Figs. 10(a), 10(b), and 10(d), dissipation terms of the even moments $\overline{u^2}$, $\overline{u^4}$ and the turbulent kinetic energy E show an approximately error-function profile across the mixing layer. However, Fig. 10(c) presents a completely different behavior for the dissipation term of the odd moment $\overline{u^3}$. In addition to it being considerably smaller in magnitude, in the vicinity of the center of the mixing layer $\eta \approx 0$, the dissipation shows an augmentation effect for $\overline{u^3}$. This observation can be explained by considering the effect of the viscosity on the PDF of u. From a statistical point of view, dissipation reduces even moments of u by reducing the width of its PDF. In the same context, dissipation increases $\overline{u^3}$ by more strongly dissipating the negative part of the PDF, i.e., $u < 0$, compared to its positive part, i.e., $u > 0$.

The motion of penetrating eddies from HIT region 1 into the mixing layer pushes the fluid in front of them and produces $u > 0$ while these penetrations from the HIT region 2 into the mixing layer produce $u < 0$. Faster decay of the latter group of eddies, which on average has relatively lower kinetic energy compared to the former group of eddies, leads to this biased effect of the dissipation on the PDF of u.

The production term $\overline{u^2}\partial_x\overline{u^3}$, which in the above equations only appears in Eq. (26), concordant with the transport term, reduces $\overline{u^4}$ in the neighborhood of the high-energy HIT region 1 ($\eta < 0$) while it has an augmentation effect in the neighborhood of the low-energy HIT region 2 ($\eta > 0$). Since $\overline{u^2}$ is positive, this behavior of the production term is originated from the behavior of $\partial_x\overline{u^3}$ inside the mixing region. Due to the isotropic condition, $\overline{u^3}$ is zero in both HIT regions 1 and 2 while within the mixing layer this quantity takes positive values. To match this profile, $\partial_x\overline{u^3}$ should be positive in the neighborhood of the high-energy HIT region 1 and negative in the neighborhood of the low-energy HIT region 2 which results in the observed profile for the production term in Fig. 10(d). However, in contrast to the transport term, the production term contributes to the total change of $\overline{u^4}$. This contribution can be found by considering the following relation:

$$\int_{\Delta(t)} \frac{\partial}{\partial x}(\overline{u^3}\,\overline{u^2})dx = \int_{\Delta(t)} \overline{u^3}\frac{\partial \overline{u^2}}{\partial x}dx + \int_{\Delta(t)} \overline{u^2}\frac{\partial \overline{u^3}}{\partial x}dx. \quad (27)$$

Using Green's theorem, the left integral is zero since $\overline{u^3}$ is zero in both HIT regions 1 and 2. Considering an approximate error-function profile for $\overline{u^2}$ throughout the mixing layer [8,47], $\partial_x\overline{u^2}$ is negative inside the mixing layer, which results in a negative value for the first integral on the right-hand side. Therefore, the second integral on the right-hand side should be always positive, which leads to an overall reduction effect of the production term on the evolution of $\overline{u^4}$.

From Fig. 10(b) and Eq. (24) it can be observed that the redistribution term has no effect on the evolution of the turbulent kinetic energy. Indeed, Eqs. (22) and (23) show that this term transfers kinetic energy between $\overline{u^2}$ and $\overline{v^2}$ without changing the total amount of the kinetic energy due to the incompressibility. Figure 10(a) shows that in the neighborhood of the low-energy HIT region 2 ($\eta > 0$), this term extracts energy from $\overline{u^2}$ and transfers it into $\overline{v^2}$. As indicated at the end of the Sec. III A, this direct contribution of $\overline{u^2}$ to

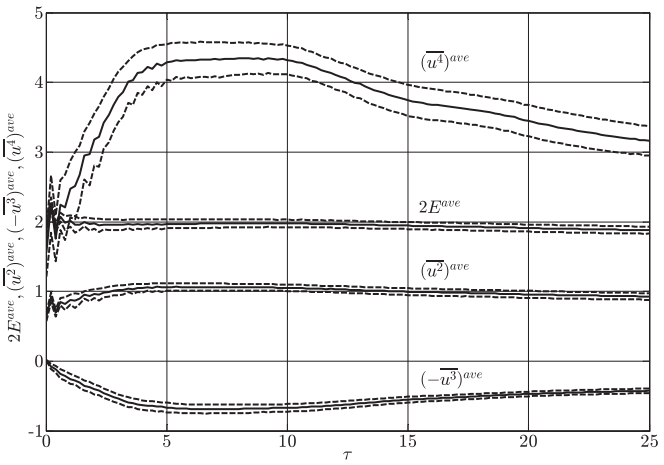

FIG. 11. Time evolutions of mean solutions and standard deviation envelopes of the averaged statistical moments. (—) Mean solution; (− − −) mean ± STD. For the sake of clarity, $(-\overline{u^3})^{\text{ave}}$ and $2E^{\text{ave}}$ are plotted instead of $(\overline{u^3})^{\text{ave}}$ and E^{ave}.

developments of $\overline{v^2}$ establishes the observed linear correlation between $K_u - K_v$ in Fig. 9(b).

The contribution of the redistribution term on the evolutions of $\overline{u^3}$ and $\overline{u^4}$ differs from that in $\overline{u^2}$. Overall, the contribution of the redistribution term in the dynamics of all velocity moments is in opposition to the transport term and might be considered the effect of the pressure drag against the penetration of energetic eddies. As explained by Briggs *et al.* [19], when energetic eddies move through the mixing layer, the fluid in front of them is pushed, which results in a positive pressure ($p > 0$) while, due to the low-pressure wake, the pressure behind penetrating eddies is negative ($p < 0$). This reverse pressure gradient exerts a force on the penetrating eddies which resists against their movements towards HIT region 2.

In Fig. 10, the location of $\eta_{\max}$ is also indicated by vertical gray line. It should be noted that both transport and redistribution terms in the HIT regions are identically zero. Therefore, nonzero values of these terms can be considered as an indication of the flow field intermittency and deviation from Gaussianity. Approximate coincidences of the transport and redistribution extremums with the location of $\eta_{\max}$ shows that, at the penetration depth, intermittency and deviation from Gaussianity are maximized.

Averaged statistical moments of the inhomogeneous velocity component and kinetic energy of the mixing region can be defined as:

$$(\overline{u^n})^{\text{ave}} \equiv \frac{1}{\Delta(t)} \int_{\Delta(t)} (\overline{u^n}) dx, \quad (n = 1,2,3,4),$$
$$E^{\text{ave}} \equiv \frac{1}{\Delta(t)} \int_{\Delta(t)} (E) dx. \tag{28}$$

Figure 11 shows mean solutions and standard deviation envelopes of time evolutions of E^{ave}, $(\overline{u^2})^{\text{ave}}$, $(\overline{u^3})^{\text{ave}}$, and $(\overline{u^4})^{\text{ave}}$, reconstructed from their corresponding gPCs. This figure shows almost stationary evolutions for $(\overline{u^2})^{\text{ave}}$, E^{ave}, and $(\overline{u^3})^{\text{ave}}$ where from approximate equality of $(\overline{u^2})^{\text{ave}}$ and E^{ave} it can be also inferred that $(\overline{v^2})^{\text{ave}} \approx (\overline{u^2})^{\text{ave}}$. Despite a considerably smaller value of $(\overline{u^3})^{\text{ave}}$ compared to the $(\overline{u^4})^{\text{ave}}$, it can be seen that time evolutions of these two intermittency quantities are qualitatively similar. Comparing the standard deviation envelope of $(\overline{u^4})^{\text{ave}}$ with those of other moments of u shows that $(\overline{u^4})^{\text{ave}}$ is more influenced by the variations of $\mathscr{E}$ and $\mathscr{L}$. Moreover, it can be seen that during the mixing layer evolution $(\overline{u^4})^{\text{ave}}$ is higher than $3(\overline{u^2})^{\text{ave}}$, which implies strong deviation from Gaussianity.

Using the Leibniz integral rule, the time derivative of any averaged quantity, ϕ^{ave}, may be evaluated as

$$\frac{d}{dt}\phi^{\text{ave}} = \frac{1}{\Delta(t)} \int_{\Delta(t)} \phi_t d\mathbf{x} + \left\{ \frac{\phi_{(+\frac{\Delta}{2})} + \phi_{(-\frac{\Delta}{2})}}{2} - \phi^{\text{ave}} \right\} \frac{\dot{\Delta}}{\Delta}, \tag{29}$$

where $\dot{\Delta}$ denotes the mixing layer growth rate ($\dot{a}$ is short for da/dt) and $\phi_{(\pm\Delta/2)}$ represents values of ϕ at the boundaries of mixing layer, i.e., HIT regions 1 and 2. In this relation, it is assumed that during the flow field evolution the mixing layer boundaries advance into HIT regions 1 and 2 with equal velocity. This approximation is examined by numerically evaluations of both sides of relation (29).

The time derivatives of E^{ave}, $(\overline{u^2})^{\text{ave}}$, $(\overline{u^3})^{\text{ave}}$, and $(\overline{u^4})^{\text{ave}}$, obtained based on this relation, are reported in Fig. 12. Considerably smaller time derivatives of E^{ave}, $(\overline{u^2})^{\text{ave}}$, $(\overline{u^3})^{\text{ave}}$ compared to that of $(\overline{u^4})^{\text{ave}}$ is consistent with the observed stationary evolutions of these statistical quantities in Fig. 11. Moreover, the qualitatively similar time evolutions of $(\overline{u^3})^{\text{ave}}$ and $(\overline{u^4})^{\text{ave}}$ in Fig. 11 can be better recognized by considering their similar dynamics in Figs. 12(c) and 12(d). From the relatively narrow bounds of the standard deviation envelopes in Figs. 12(a)–12(d), it can be concluded that dynamics of these statistical moments are not substantially affected by variations of $\mathscr{L}$ and $\mathscr{E}$.

The sensitivities of the dynamics of E^{ave}, $(\overline{u^2})^{\text{ave}}$, $(\overline{u^3})^{\text{ave}}$, and $(\overline{u^4})^{\text{ave}}$ to the variations of $\mathscr{E}$ and $\mathscr{L}$ are reported in Fig. 13. Similarly to the previous observations, $\mathscr{E}$ has the dominant effect on the variabilities of the dynamics of these statistical quantities. Further, it can be observed that by increasing the order n in $(\overline{u^n})^{\text{ave}}$, the contribution of $\mathscr{E}$ on the variability of the dynamics of $(\overline{u^n})^{\text{ave}}$ reduces while the contributions of $\mathscr{L}$ and its interaction with $\mathscr{E}$ increases.

C. Mixing layer evolution

In this section, the impact of the variations of initial condition parameters on the thickness growth of the mixing layer, stretching and folding of material lines, and mixing efficiency are investigated. Notably, it has been found that, in contrast to the intermittency statistics, increasing $\mathscr{E}$ shows hampering effects on the evolutions of the above-mentioned mixing parameters.

This contradictory effect can be attributed to the dependency of the random motions of the energetic eddies on the Reynolds number. The energetic eddies of the adjacent HIT regions sporadically penetrate into the mixing region and agitate the flow field inside the mixing region. Increasing the Reynolds number can augment these random motions, leading to the increase of the recurrence of these penetrations and intensification of the agitation process.

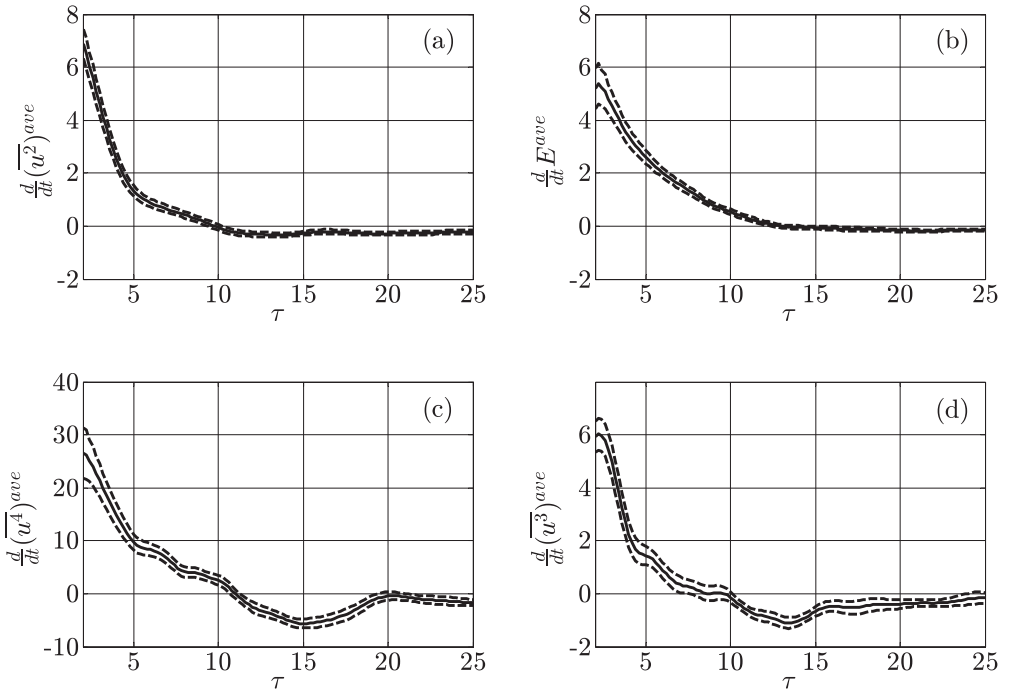

FIG. 12. Mean solutions and standard deviation envelopes of the growth rate of the averaged statistical moments (a) $d(\overline{u^2})^{\text{ave}}/dt$, (b) dE^{ave}/dt, (c) $d(\overline{u^4})^{\text{ave}}/dt$, and (d) $d(\overline{u^3})^{\text{ave}}/dt$. (—) Mean solution; $(- - -)$ mean $\pm$ STD.

The Reynolds numbers of two adjacent HIT regions 1 and 2 can be related as $\text{Re}_2 = \text{Re}_1/(\sqrt{\mathscr{E}}\mathscr{L})$. Since the turbulent state of the HIT region 1 is kept constant, it can be observed that reduction of $\mathscr{E}$ and $\mathscr{L}$ increases the Reynolds number of the HIT region 2.

1. Thickness layer growth

As already noted, the mixing layer thickness $\Delta(t)$ can be defined as the distance between the points with scalar $0.25 \leqslant Z(\mathbf{x},t) \leqslant 0.75$. This length represents the extent of the region with a significant level of anisotropy. Initially, all the

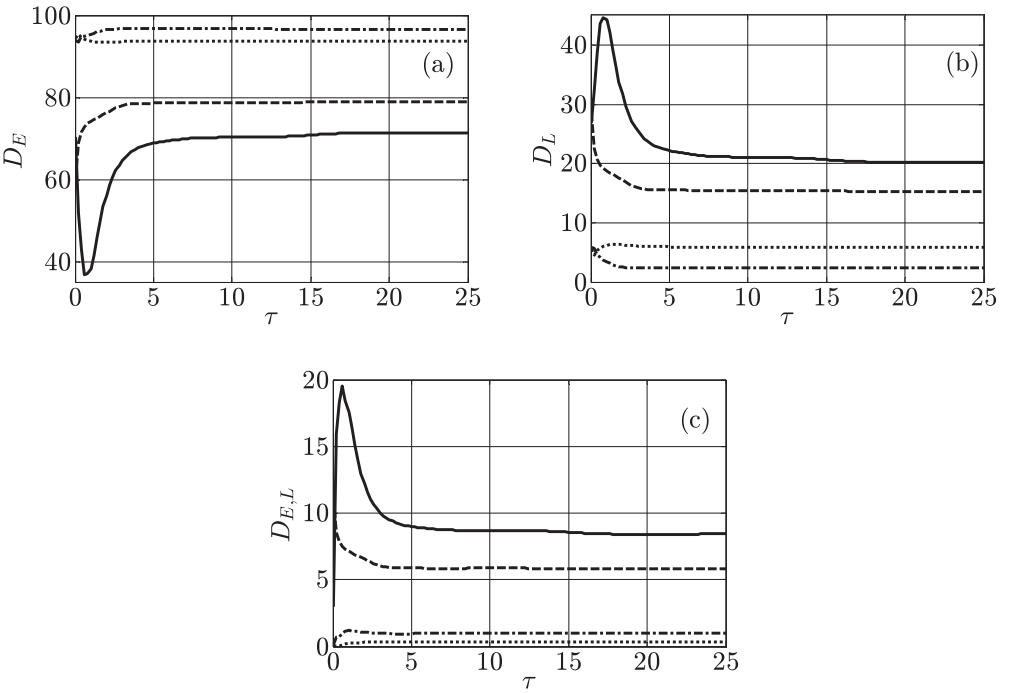

FIG. 13. Time evolutions of the Sobol's sensitivity indices with respect to the variations of (a) energy ratio, (b) integral length scale ratio, and (c) interaction of their covariation; (—): $d(\overline{u^4})^{\text{ave}}/dt$, (- - -): $d(\overline{u^3})^{\text{ave}}/dt$, $(- \cdot -)$: $d(\overline{u^2})^{\text{ave}}/dt$, and $(\cdots)$: dE^{ave}/dt.

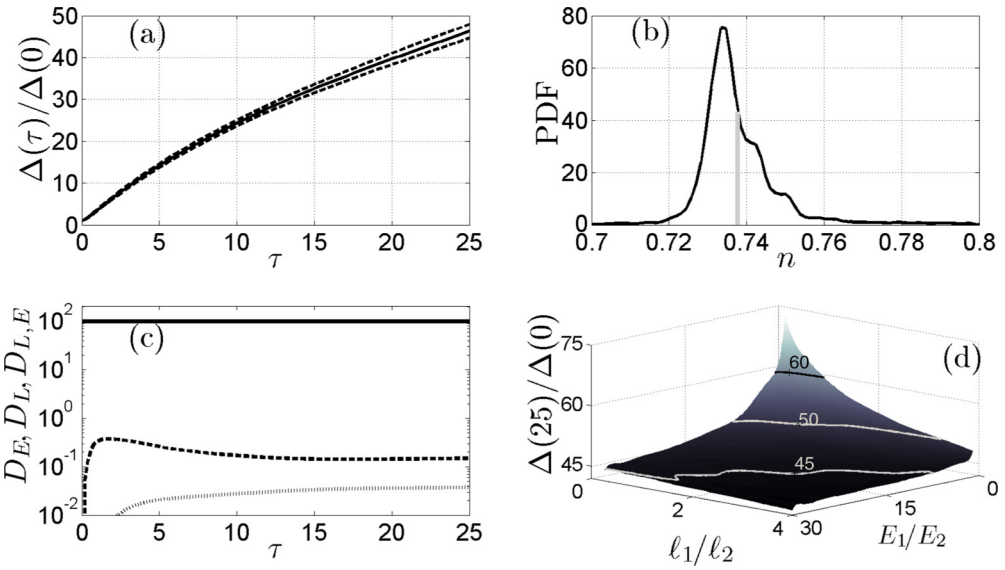

FIG. 14. Time evolution of the normalized mixing layer thickness. (a) The mean solution and standard deviation envelope; (—) mean solution; (− − −) mean ± STD. (b) PDF of the growth-rate power-law exponent $n = d\ln[\Delta(t)]/d\ln t$. (c) Sobol's sensitivity indices for the variation of the mixing layer thickness with respect to the variations of (—) energy ratio, integral length scale ratio, and (···) interaction of their covariation. (d) Response surface of the final thickness of the mixing layer as a function of $\mathscr{E}$ and $\mathscr{L}$.

mixing layers have identical thicknesses $\Delta(0) = L/800$ while, at the end of the simulations, mixing layer thicknesses vary as $0.05L \leqslant \Delta(25) \leqslant 0.09L$.

Figure 14 reports different information about the growth of the mixing layer thickness. In Fig. 14(a), time evolution of the mean solution and the standard deviation envelope of the normalized mixing layer thickness is shown. A power-law growth for the mixing layer thickness evolution can be observed which is equivalent to a linear growth in a logarithmic scale. The PDF of the slope of this linear growth in logarithmic scale, defined as $n = d\ln[\Delta(t)]/d\ln t$, is presented in Fig. 14(b). From this PDF it can be observed that the growth-rate exponent n is mainly between 0.72 and 0.78 with a mean value of $n_{\text{ave}} = 0.73$. The relatively narrow width of this PDF shows that the mixing layer growth is relatively insensitive to the variations of the initial condition parameters $\mathscr{L}$ and $\mathscr{E}$. The sensitivity indices, reported in Fig. 14(c), reveal that despite robust dynamics of the mixing layer growth, almost 99% of the variability of the growth rate originates from variation of $\mathscr{E}$. Figure 14(d) shows the reconstructed response surface of the final mixing layer thickness normalized by the initial thickness, i.e., $\Delta(\tau = 25)/\Delta(\tau = 0)$. It can be observed that the maximum spread of the mixing layer takes place at the lowest initial energy ratio $\mathscr{E} = 1$ and initial length scale ratio $\mathscr{L} = 1/4$.

In this initial length scale ratio, HIT region 2 has the largest integral length scale and, consequently, the lowest turbulent kinetic energy decay rate. Therefore, the $\text{Re}_2 = \sqrt{E_2(t)}\ell_2(t)/\nu$, has the highest magnitude during flow field evolution. Increasing the integral length scale ratio $\mathscr{L}$ results in a smaller integral length scale of the homogeneous region 2 and, consequently, a higher turbulent kinetic energy decay rate.

2. *The scalar front and mixing efficiency*

Kinematically, fluid mixing can be considered as the stretching and folding of material lines and surfaces when they are subjected to the induced strain field of the adjacent vortical structures. To quantify this stretching and folding process, the length and the mean curvature of the scalar isolevel contour $Z = 0.5$, hereafter denoted as scalar front, are considered, i.e.,

$$\Lambda = \oint_{Z=0.5} dx, \quad \text{and} \quad \kappa_{\text{ave}} = \frac{1}{\Lambda}\oint_{Z=0.5} \underbrace{\text{abs}(\nabla\cdot\mathbf{n})}_{\kappa} dx, \tag{30}$$

where $\mathbf{n} = \nabla Z/|\nabla Z|$ is the normal vector to the scalar front with a direction toward the center of the curvature (or center of the osculating circle). Figure 15 shows time evolutions of the normalized scalar front length, $\Lambda(\tau)/\Lambda(0)$, and its mean curvature κ_{ave}. Figure 15(a) shows that, similarly to the three-dimensional turbulence, as the result of chaotic stretching, the mean solution of the scalar front length and its standard deviation envelope monotonically increase during the flow field evolution. Figure 15(b) shows the mean solution κ_{ave} and its standard deviation envelope. It can be observed that the front curvature, which represents the corrugation of the scalar front elements, increases during an initial transition period and afterwards, during the well-developed stage of the flow field evolution, i.e., $10 \leqslant \tau \leqslant 25$, undergoes monotonic reduction.

The rate of the material line filamentation is controlled by the strain field of the adjacent large-scale eddies while the strain field of the small scale eddies simply wrinkles the material line. During the initial transition period $\tau \leqslant 10$, in which vorticity field includes large- and small-scale eddies, material lines are subjected to the strain fields of both large- and small-scale eddies which result in simultaneous growth in the length and curvature of the material lines. At the end of this transition period, turbulence adjusts to its fully developed state in which the inverse energy cascade from the small

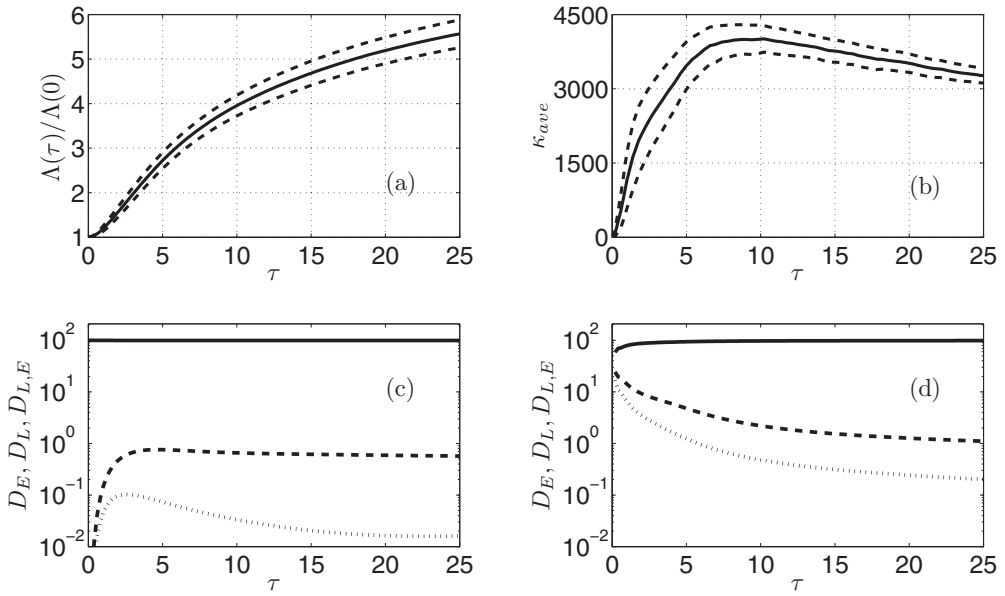

FIG. 15. Mean solutions and standard deviation envelops for the scalar isolevel $Z = 0.5$ (a) normalized length and (b) its average curvature. (—) Mean solution; (− − −) mean ± STD. Sobol's sensitivity indices for the variations of (c) the scalar front length and (d) the average of its curvature with respect to the variations of (—) energy ratio, (− − −) integral length scale ratio, and (· · ·) interaction of their covariation.

scales to the large scales results in vortex merging process and continual growth in the size of eddies. Accordingly, after $\tau \geqslant 10$, material lines are mainly influenced by the strain field of the large-scale eddies and continue to extend while their curvature reduces.

Figures 15(c) and 15(d) show Sobol's sensitivity indices for the variations of the normalized scalar front length and its mean curvature with respect to the variations of $\mathscr{E}$ and $\mathscr{L}$. It can be observed that above 90% of variations of both quantities are originated from variations of $\mathscr{E}$ while variations of $\mathscr{L}$ and its interaction with $\mathscr{E}$ have negligible effect on stretching and folding process. Regarding the observed opposite tendency between stretching and bending mechanism in Figs. 15(a) and 15(b), a relation between the overall length of the material line and its average curvature is south in Fig. 16. By examining the time evolution of $\Lambda \cdot \kappa_{\text{ave}}$, it is immediately apparent

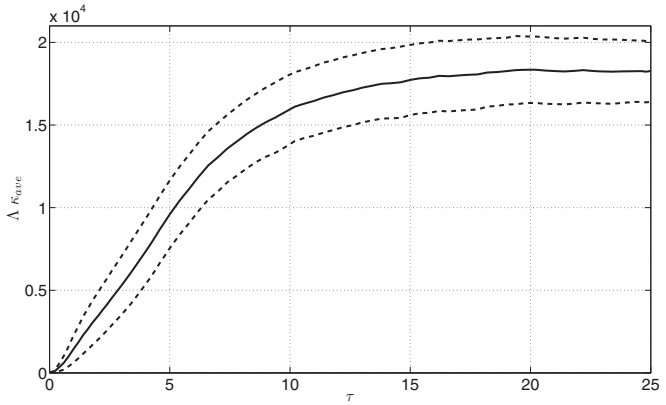

FIG. 16. Time evolution of $(\Lambda \cdot \kappa_{\text{ave}})$ for the scalar isolevel $Z = 0.5$; (—) mean solution; (− − −) mean ± STD.

that during the well-developed stage, i.e., $\tau \geqslant 10$, the mean solution of this quantity and its standard deviation envelope show an almost constant evolution, which means the length of the material line and its average curvature are nearly anticorrelated, i.e., $\Lambda \propto {\kappa_{\text{ave}}}^{-1}$. Related to this observation, Drummond [48] and Thiffeault [49] reported that for a material line segment high curvature regions are consistently associated with low stretching with exponent $-1/3$.

Response surfaces of the final scalar front length normalized by the initial length and its average curvature are also demonstrated in Figs. 17(a) and 17(b). It can be observed in Fig. 17(b) that the final scalar front length is a decreasing function of both $\mathscr{E}$ and $\mathscr{L}$, i.e., the largest final scalar front length is at $\mathscr{E} = 1$ and $\mathscr{L} = 1/4$. Figure 17(a) shows that the final average curvature is also a decreasing function of $\mathscr{E}$; however, unlike the scalar front length, it increases by increasing $\mathscr{L}$. This issue is visualized in Fig. 4, i.e., $\mathscr{E}$=1, in which interface structure becomes more intricate by increasing $\mathscr{L}$.

Closely related to the stretching process, mixing efficiency of the flow field can be quantified based on the normalized material line growth,

$$e = \frac{1}{\Delta(t)} \int_{\Delta(t)} \overline{\left(\frac{l_i l_j s_{ij}}{\sqrt{s_{ij} s_{ij}}} \right)} dx, \tag{31}$$

where $l_i = dx_i/|dx_i|$ is the orientation vector of the material line $|dx|$ and $s_{ij} = (\partial_j u_i + \partial_i u_j)/2$ is the strain rate tensor [50]. It can be shown that for an incompressible two-dimensional flow, the integrand in (31) can be simplified to $(\sqrt{2}/2)\overline{\cos(2\alpha)}$, where α is the angle between the material line alignment l_i and the stretching eigenvector of the strain rate tensor [51]. This simplified equation provides an upper bound $\sqrt{2}/2 \approx 0.707$ for the mixing efficiency in an incompressible two-dimensional flow.

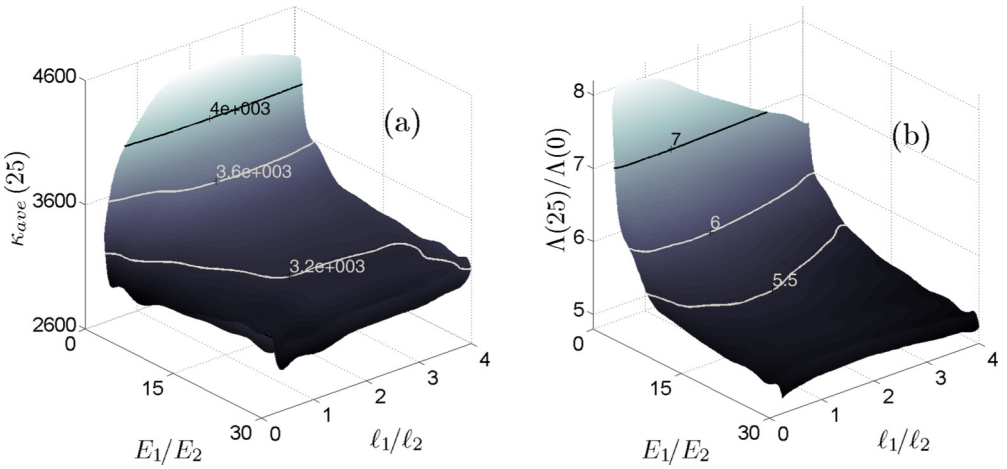

FIG. 17. Response surfaces for the final (a) averaged curvature and (b) length of the scalar isolevel $Z = 0.5$ as a function of $\mathscr{E}$ and $\mathscr{L}$.

Figure 18(a) shows the time evolution of the mean solution of the mixing efficiency e and its standard deviation envelope. It can be observed that after an initial transitional period, i.e., $\tau \sim 10$, the mixing efficiency develops to an almost constant level $e \sim 0.2$, which is considerably lower than the maximum efficiency $\sqrt{2}/2 \approx 0.707$.

Figure 18(b) presents the PDF of the mixing efficiency during the almost-stationary period $10 \leqslant \tau \leqslant 25$. The mixing efficacy shows a Gaussian-like distribution between 0.19 and 0.21, in which the mean value is indicated with a gray vertical bar. The relatively compact PDF in Fig. 18(b) and corresponding narrow bound of the standard deviation envelope in Fig. 18(a) imply that the mixing efficiency has relatively low sensitivity to the variations of the initial parameters $\mathscr{E}$ and $\mathscr{L}$. However, using Sobol's sensitivity index, it is found that, similarly to the growth of the scalar front in Fig. 17(c), almost 99% of the mixing efficiency variations is originated from variations of initial $\mathscr{E}$ (results not shown).

In Fig. 18(c) the reconstructed response surface for the time-averaged mixing efficiency is presented, i.e., $e_T = (\int_T e\,dt)/T$, where $T \in [10\ 25]$. The reconstructed response surface shows smooth monotonic increase with increasing $1/\mathscr{E}$ and $\mathscr{L}$ with maximum of the mixing efficiency at $\mathscr{E} = 1$, $\mathscr{L} = 4$. Moreover, it can be clearly observed that variations of the initial condition parameters $\mathscr{E}$ and $\mathscr{L}$ lead to approximately 10% variation of the mixing efficiency. It should be noted that the time-averaged mixing efficiency can be interpreted as the Lyapunov exponent of the particle trajectories which quantifies the divergence of initially adjacent fluid particles during the flow field evolution.

Considering Figs. 17 and 18, it can be observed that decreasing $\mathscr{E}$ has an augmentation effect on all indications of

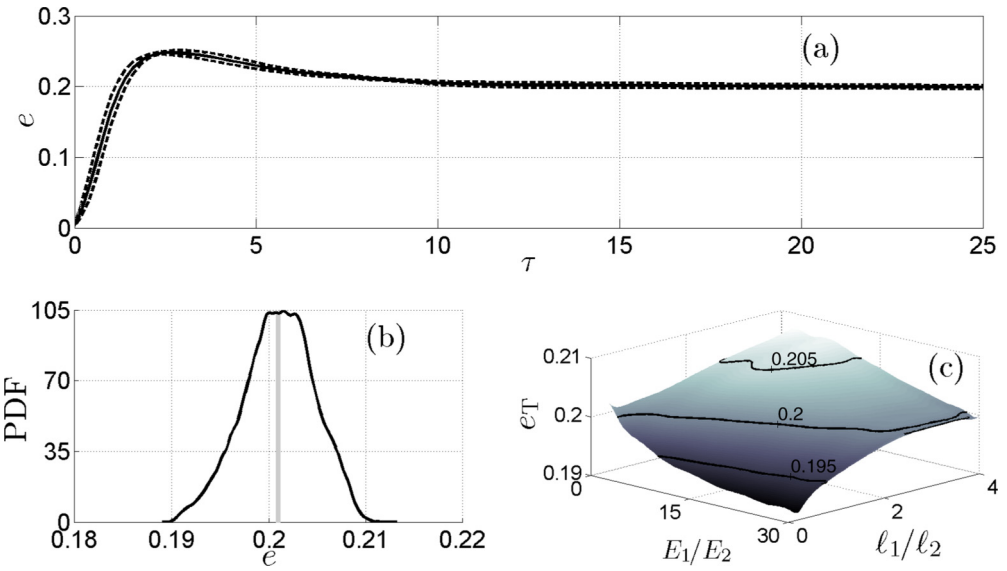

FIG. 18. The mixing efficiency inside the mixing region. (a) Time evolution of the mean solution and standard deviation envelope of the mixing efficiency; (—) mean solution; (− − −) mean ± STD. (b) PDF of the mixing efficiency with the average value of 0.201, indicated by the gray line. (c) Response surface of the time averaged mixing efficiency, $e_T = (\int_T e\,dt)/T$, as a function of $\mathscr{E}$ and $\mathscr{L}$. Time interval for the presented quantities in (b) and (c) is $10 \leqslant \tau \leqslant 25$.

the mixing, i.e., the scalar front final length, $\Lambda(25)$, the average curvature $\kappa_{ave}(25)$, and the mixing efficiency. However, among these quantities, only the scalar front final length $\Lambda(25)$ increases with increasing $\mathscr{L}$ while the other quantities show opposite trends.

IV. CONCLUSION

The sensitivity of the temporal evolution of a two-dimensional incompressible shearless turbulent mixing layer to the variations of initial condition parameters is investigated using DNS and gPC representation. Initial integral length scales and turbulent kinetic energies of two interacting HIT fields are considered as the controlling parameters for the subsequent (a) flow field intermittency and departure from Gaussianity, (b) energy transfer mechanisms, and (c) mixing efficiency of the mixing layer.

It is found that all of the above-mentioned aspects of the flow field evolution are influenced by the ratio of the initial energy and integral length scales, i.e., $\mathscr{E} = E_1(0)/E_2(0)$ and $\mathscr{L} = \ell_1(0)/\ell_2(0)$. However, dependency of flow field intermittency and energy transfer mechanisms inside the mixing region on $\mathscr{E}$ and $\mathscr{L}$ differs from that of mixing process parameters.

To perform sensitivity analysis, a DNS database solution has been produced by considering the controlling parameters as IID random variables with uniform distribution over the parametric domain $1/4 \leqslant \mathscr{L} \leqslant 4$ and $1 \leqslant \mathscr{E} \leqslant 30$. Subsequently, by stochastic gPC representation of discrete DNS solution samples, different flow field quantities are expressed as continuous functions of controlling parameters $\mathscr{L}$ and $\mathscr{E}$.

The study of the sensitivity indices shows that the most influential parameter on the variability of all of the above-mentioned aspects of the shearless mixing layer evolution is $\mathscr{E}$. Variation of $\mathscr{L}$ has considerably lower impact on the flow field variability compared to the $\mathscr{E}$. The interaction between $\mathscr{L}$ and $\mathscr{E}$ shows negligible contributions on the total variations of flow field parameters, which means that influence of the two controlling parameters on the overall flow field evolution is almost additive.

Similarly to the three-dimensional flow field, the two-dimensional shearless mixing layer is also highly intermittent and velocity statistics show significant deviation from Gaussian distribution. This intermittency can be discerned in both large and small scales. Large-scale intermittency is measured by considering the skewness and the kurtosis of the velocity field. Moreover, the structure of the two-dimensional shearless mixing layer anisotropy establishes particular correlations between the velocity skewness and kurtosis, similar to those in the three-dimensional shearless mixing layers. The small-scale intermittency is examined based on the velocity derivative skewness and kurtosis. Comparing large and small scales, it is found that the former group shows higher levels of intermittency and larger variability compared to the latter group. The small-scale intermittency develops to an almost constant value while the large-scale intermittency shows different behavior. It is observed that for mixing layers with imposed $\mathscr{L} > 1$, the mixing region intermittency and turbulent penetration depth increases during the flow field evolution while $\mathscr{L} < 1$ leads to an opposite effect.

Time evolutions of velocities moments up to order three do not show significant variability and sensitivity to the variations of $\mathscr{L}$ and $\mathscr{E}$. All of these moments develop to an almost stationary evolutions with magnitude independent from controlling parameters $\mathscr{L}$ and $\mathscr{E}$. Contrariwise, the fourth-order velocity moment does not achieve to a stationary state and its evolution shows higher variability in comparison with the lower velocity moments.

In all cases, the mixing region shows a power-law growth during the flow field evolution. The growth rate, measured by its slope, n, in the logarithmic scale, shows variations within the range $0.72 \leqslant n \leqslant 0.78$ in response to the variations of $\mathscr{L}$ and $\mathscr{E}$. It is found that variations of the growth rate is a decreasing function of $\mathscr{E}$ and $\mathscr{L}$. Finally, the mixing efficiency inside the mixing region shows an almost stationary evolution with magnitude $0.19 \leqslant e \leqslant 0.21$ with a monotonic dependence on both $1/\mathscr{E}$ and $\mathscr{L}$.

[1] E. Balaras, U. Piomelli, and J. M. Wallace, J. Fluid Mech. **446**, 1 (2001).
[2] W. K. George and L. Davidson, AIAA J. **42**, 438 (2004).
[3] P. Tabeling, Phys. Rep. **362**, 1 (2002).
[4] S. Fox and P. A. Davidson, J. Fluid Mech. **659**, 351 (2010).
[5] G. Boffetta and R. E. Ecke, Annu. Rev. Fluid Mech. **44**, 427 (2012).
[6] H. Kellay and W. I. Goldburg, Rep. Prog. Phys. **65**, 845 (2002).
[7] C.-M. Ho and P. Huerre, Annu. Rev. Fluid Mech. **16**, 365 (1984).
[8] S. Veeravalli and Z. Warhaft, J. Fluid Mech. **207**, 191 (1989).
[9] A. Hussain and M. F. Zedan, Phys. Fluids **21**, 1475 (1978).
[10] M. M. Rogers and R. D. Moser, J. Fluid Mech. **243**, 183 (1992).
[11] R. D. Moser and M. M. Rogers, J. Fluid Mech. **247**, 275 (1993).
[12] M. M. Rogers and R. D. Moser, Phys. Fluids **6**, 903 (1994).
[13] P. Druault, S. Lardeau, J. P. Bonnet, F. Coiffet, J. Delville, E. Lamballais, J. F. Largeau, and L. Perret, AIAA J. **42**, 447 (2004).
[14] F. K. Browand and B. O. Latigo, Phys. Fluids **22**, 1011 (1979).
[15] B. Dziomba and H. E. Fiedler, J. Fluid Mech. **152**, 419 (1985).
[16] J. H. Bell and R. D. Mehta, AIAA J. **28**, 2034 (1990).
[17] J. Ko, D. Lucor, and P. Sagaut, Phys. Fluids **20**, 077102 (2008).
[18] M. Zayernouri and M. Metzger, Phys. Fluids **23**, 025105 (2011).
[19] D. A. Briggs, J. H. Ferziger, J. R. Koseff, and S. G. Monismith, J. Fluid Mech. **310**, 215 (1996).
[20] M. Fathali, J. Meyers, G. Rubio, S. Smirnov, and M. Baelmans, J. Turb. **9**, 1 (2008).
[21] B. Gilbert, J. Fluid Mech. **100**, 349 (1980).
[22] B. Knaepen, O. Debliquy, and D. Carati, J. Fluid Mech. **514**, 153 (2004).
[23] D. Tordella and M. Iovieno, J. Fluid Mech. **549**, 429 (2006).
[24] H. S. Kang and C. Meneveau, Phys. Fluids **20**, 125102 (2008).
[25] D. Tordella and M. Iovieno, Phys. Rev. Lett. **107**, 194501 (2011).
[26] D. Tordella and M. Iovieno, Physica D **241**, 178 (2012).

[27] M. Iovieno, S. D. Savino, L. Gallana, and T. Tordella, J. Turb. **15**, 311 (2014).
[28] D. Xiu and G. E. Karniadakis, SIAM J. Sci. Comput. **24**, 619 (2002).
[29] D. Xiu and G. E. Karniadakis, J. Comput. Phys. **187**, 137 (2003).
[30] R. Ghanem and P. D. Spanos, *Stochastic Finite Elements: A Spectral Approach* (Dover, London, 2003).
[31] O. Knio and O. Le Maitre, Fluid Dyn. Res. **38**, 616 (2006).
[32] O. P. Le Maitre and O. M. Knio, *Spectral Methods for Uncertainty Quantification: With Applications to Computational Fluid Dynamics* (Springer, Berlin, 2010).
[33] J. R. Chasnov, Phys. Fluids **9**, 171 (1997).
[34] P. A. Davidson, *Turbulence: An Introduction for Scientists and Engineers: An Introduction for Scientists and Engineers* (Oxford University Press, Oxford, 2004).
[35] A. J. Lowe and P. A. Davidson, Eur. J. Mech. B/Fluids **24**, 314 (2005).
[36] A. S. Monin and A. M. Yaglom, *Statistical Fluid Mechanics, Volume II: Mechanics of Turbulence*, Vol. 2 (MIT Press, Cambridge, MA, 1975).
[37] D. G. Fox and S. A. Orszag, J. Comput. Phys. **11**, 612 (1973).
[38] N. Wiener, Am. J. Math. **60**, 897 (1938).
[39] D. Xiu, *Numerical Methods for Stochastic Computations: A Spectral Method Approach* (Princeton University Press, Princeton, NJ, 2010).
[40] B. Carnahan, H. A. Luther, and J. O. Wilkes, *Applied Numerical Methods* (John Wiley & Sons, New York, 1969).
[41] I. M. Sobol, Math. Modell. Comp. Exp. **1**, 407 (1993).
[42] A. Tsinober, *An Informal Conceptual Introduction to Turbulence* (Springer, Berlin, 2009).
[43] S. Pope, *Turbulent Flows* (Cambridge University Press, Cambridge, 2005).
[44] L. Biferale, S. Musacchio, and F. Toschi, J. Fluid Mech. **730**, 309 (2013).
[45] D. Tordella, M. Iovieno, and P. R. Bailey, Phys. Rev. E **77**, 016309 (2008).
[46] R. Betchov, J. Fluid Mech. **1**, 497 (1956).
[47] S. B. Pope and D. C. Haworth, Turb. Shear Flows **5**, 44 (1986).
[48] I. T. Drummond, J. Fluid Mech. **252**, 479 (1993).
[49] J. L. Thiffeault, Physica D **198**, 169 (2004).
[50] J. M. Ottino, *The Kinematics of Mixing: Stretching, Chaos, and Transport* (Cambridge University Press, Cambridge, 2005).
[51] B. Protas, A. Babiano, and N. K.-R. Kevlahan, Physica D **128**, 169 (1999).